Dynamics of the peptidoglycan biosynthetic machinery in the stalked budding bacterium *Hyphomonas neptunium*

Emöke Cserti[a,b], Sabine Rosskopf[a], Yi-Wei Chang[c], Sabrina Eisheuer[a,b], Lars Selter[d], Jian Shi[c,#], Christina Regh[a], Ulrich Koert[d], Grant J. Jensen[c,e], Martin Thanbichler[a,b,f]

[a] Faculty of Biology, Philipps-Universität, 35043 Marburg, Germany, [b] Max Planck Institute for Terrestrial Microbiology, 35043 Marburg, Germany, [c] Division of Biology and Bioengineering, California Institute of Technology, Pasadena, CA 91125, USA, [d] Faculty of Chemistry, Philipps-Universität, Marburg, Germany, [e] Howard Hughes Medical Institute, California Institute of Technology, Pasadena, CA 91125, USA, and [f] LOEWE Center for Synthetic Microbiology, 35043 Marburg, Germany

[#] current address: NUS Centre for BioImaging Sciences, National University of Singapore, Singapore 117557

Key words:
Polar growth, stalked bacteria, morphogenesis, *Agrobacterium*, *Caulobacter*

Running title:
Morphogenesis of *Hyphomonas neptunium*

For correspondence:
Martin Thanbichler
E-mail: thanbichler@uni-marburg.de
Phone: +49-6421-2821809
Fax: +49-6421-2821832

SUMMARY

Most commonly studied bacteria grow symmetrically and divide by binary fission, generating two siblings of equal morphology. An exception to this rule are budding bacteria, in which new offspring emerges *de novo* from a morphologically invariant mother cell. Although this mode of proliferation is widespread in diverse bacterial lineages, the underlying mechanisms are still incompletely understood. Here, we perform the first molecular-level analysis of growth and morphogenesis in the stalked budding alphaproteobacterium *Hyphomonas neptunium*. Peptidoglycan labeling shows that, in this species, buds originate from a stalk-like extension of the mother cell whose terminal segment is gradually remodeled into a new cell compartment. As a first step toward identifying the machinery mediating the budding process, we performed comprehensive mutational and localization studies of predicted peptidoglycan biosynthetic proteins in *H. neptunium*. These analyses identify factors that localize to distinct zones of dispersed and zonal growth, and they suggest a critical role of the MreB-controlled elongasome in cell morphogenesis. Collectively, our work shows that the mechanism of growth in *H. neptunium* is distinct from that in related, polarly growing members of the order *Rhizobiales*, setting the stage for in-depth analyses of the molecular principles regulating the fascinating developmental cycle of this species.

INTRODUCTION

Bacteria have evolved a variety of shapes and sizes, which improve fitness in the environments they inhabit (Young, 2006). However, despite decades of intensive research, the mechanisms controlling bacterial morphogenesis and the selective advantages provided by particular morphologies are still incompletely understood.

In most bacteria, cell shape is determined by a cell wall made of peptidoglycan (PG), a mesh-like polymer that encompasses the entire cell and provides resistance against the internal osmotic pressure (Vollmer *et al.*, 2008; Typas *et al.*, 2012). PG consists of a glycan backbone composed of strands of alternating *N*-acetylglucosamine (GlcNAc) and *N*-acetylmuramic acid (MurNAc) subunits. These glycan strands are interconnected by peptide bridges that are attached to the MurNAc moieties, giving rise to a single elastic macromolecule known as the murein sacculus (Schleifer and Kandler, 1972). Cell wall biogenesis is mediated by a sophisticated and highly conserved machinery (Typas *et al.*, 2012). Initially, the PG precursor lipid II is synthesized in several steps in the cytoplasm (Bouhss *et al.*, 2008). First, an L-Ala^{1}–D-Glu^{2}–L-Lys/*meso*-DAP^{3}–D-Ala^{4}–D-Ala^{5} pentapeptide side chain (stem peptide) is attached to a UDP-linked MurNAc residue (Vollmer and Bertsche, 2008). After transfer of the muramyl pentapeptide moiety to the membrane carrier bactoprenol and subsequent addition of GlcNAc, the resulting lipid II molecule (van Heijenoort, 2001) is flipped across the cytoplasmic membrane (Mohammadi *et al.*, 2011; Sham *et al.*, 2014). In the periplasm, synthetic transglycosylases (GTases) form a β-1,4-glycosidic bond between the GlcNAc moiety of lipid II and the terminal MurNAc moiety of a nascent glycan chain, thereby incorporating the precursor molecule into the existing sacculus. Concomitantly, the peptide side chains of newly synthesized glycan strands are crosslinked by transpeptidases (TPases) (Vollmer and Bertsche, 2008), also known as penicillin-binding proteins (PBPs) (Suginaka *et al.*, 1972).

Based on their domain composition, PG synthases can be divided into three distinct groups: bifunctional GTases/TPases (class A PBPs), monofunctional TPases (class B PBPs) and monofunctional GTases (Vollmer and Bertsche, 2008). *Escherichia coli* possesses three bifunctional PG synthases (PBP1A, PBP1B, and PBP1C), one GTase (MtgA) and two monofunctional TPases, of which PBP2 is essential for cell elongation and PBP3 (also known as FtsI) is essential for cell division (Spratt, 1975). Most TPases are D,D-transpeptidases, which catalyze D-Ala^{4}–*meso*-DAP^{3} crosslinks (4,3-crosslinks) (Glauner *et al.*, 1988). Alternatively, crosslinks can be formed between two *meso*-DAP residues (3,3-crosslinks), in a reaction catalyzed by specialized L,D-transpeptidases (LDTs) (Magnet *et al.*, 2008). Due to their β-lactam insensitivity, these enzymes can constitute a fail-safe mechanism to compensate for the loss of D,D-

transpeptidase activity in the presence of β-lactam antibiotics (Mainardi *et al.*, 2005). However, in certain species, LDTs may also form an integral part of the generic PG biosynthetic machinery. For instance, recent work has suggested that they critically contribute to cell elongation in *Agrobacterium tumefaciens*, a member of the *Rhizobiales*, by mediating the characteristic polar growth of this species (Brown *et al.*, 2012; Cameron *et al.*, 2014; Grangeon *et al.*, 2015).

Growth and cell division require continuous remodeling of the PG meshwork, which includes the cleavage of the existing PG meshwork to make space for the insertion of new cell wall material. This process is mediated by several distinct groups of PG-degrading enzymes, including amidases, peptidases, and lytic transglycosylases (Höltje, 1995). N-acetylmuramyl-L-alanine amidases remove the peptide side chains from the glycan backbone (Van Heijenoort and Van Heijenoort, 1971), whereas carboxy- and endopeptidases cleave diverse bonds within the stem peptides or the crosslink that connects two peptide side chains (Höltje, 1995). Lytic transglycosylases, by contrast, shorten glycan strands by cleaving the ß-1,4-glycosidic bond between MurNAc and GlcNAc, generating 1,6-anhydromuropeptides that are recycled to synthesize new PG precursors (Höltje *et al.*, 1975; Scheurwater *et al.*, 2008).

The activities of PG synthases and hydrolases need to be closely coordinated in time and space to preserve the integrity of the cell wall and thus prevent cell lysis. To this end, synthetic and lytic factors are thought to assemble into large multi-protein complexes, in which they modify the PG meshwork in a regulated and synchronized manner (Höltje, 1998; Nguyen *et al.*, 2015). In recent years, at least two such machineries have been identified, called the elongasome and the divisome (Typas *et al.*, 2012). The elongasome is found in most rod-shaped bacteria and mediates the incorporation of PG along the lateral walls of the cell. Its function is thought to be controlled by the actin homolog MreB (Jones *et al.*, 2001; van den Ent *et al.*, 2001; Daniel and Errington, 2003), which forms patch- or arc-like filaments that are tethered to the inner face of the cytoplasmic membrane (Dominguez-Escobar *et al.*, 2011; Garner *et al.*, 2011; Salje *et al.*, 2011; van Teeffelen *et al.*, 2011; Swulius and Jensen, 2012; Olshausen *et al.*, 2013). These structures interact with the inner-membrane protein RodZ (Shiomi *et al.*, 2008; Alyahya *et al.*, 2009; Bendezu *et al.*, 2009), which in turn links them, directly or indirectly, to an elongation-specific PG biosynthetic complex containing the monofunctional TPase PBP2 (Typas *et al.*, 2012; Lee *et al.*, 2014; Morgenstein *et al.*, 2015).

At the onset of cell division, the divisome takes over the control of PG biosynthesis to coordinate pre-septal cell elongation and, subsequently, constriction of the cell at the division plane (Lutkenhaus *et al.*, 2012). Among the numerous components of this envelope-spanning multiprotein complex that is

controlled by the tubulin homolog FtsZ are a variety of PG synthases and hydrolases (Typas *et al.*, 2012), including the division-specific monofunctional TPase FtsI (PBP3) (Weiss *et al.*, 1999). Together, they coordinately remodel the cell wall to generate the new polar caps of the cell. Notably, in *E. coli* and *Caulobacter crescentus*, MreB relocates from its lateral positions to the division site before the onset of cell constriction, suggesting a link between the elongasome and divisome during some stages of the division cycle (Figge *et al.*, 2004; Fenton and Gerdes, 2013). Although the enzyme families involved in PG biogenesis are conserved among bacteria, the nature of the proteins involved and the regulatory pathways controlling their activity vary considerably between different bacterial lineages. Therefore, our knowledge on the mechanisms of bacterial morphogenesis is still far from complete.

In many rod-shaped bacteria such as the model species *E. coli* and *B. subtilis*, the combined action of the elongasome and divisome leads to symmetric cell wall synthesis, resulting in the formation of two equally sized daughter cells (Typas *et al.*, 2012; Randich and Brun, 2015). However, there are also alternative ways to guide cell wall synthesis that lead to an asymmetric pattern of PG incorporation. During cell elongation in rod-shaped and filamentous actinobacteria, for instance, new PG is exclusively inserted at the cell poles (Flärdh, 2003; Cameron *et al.*, 2015). This process is governed by the polar scaffolding protein DivIVA, a factor strictly limited to Gram-positive bacteria (Flärdh, 2003; Letek *et al.*, 2009; Joyce *et al.*, 2012). Highly asymmetric growth patterns are also widespread among Gram-negative alphaproteobacteria, especially among members of the orders *Rhizobiales* and *Caulobacterales* (Randich and Brun, 2015) (**Fig. 1**). Notably, *Rhizobiales* lack MreB and other elongasome components such as MreCD, RodA, RodZ, and PBP2 (Margolin, 2009; Brown *et al.*, 2012). Their rod-shaped representative *A. tumefaciens* and related species of the families *Rhizobiaceae* and *Brucellaceae* were recently shown to elongate exclusively by tip extension before dividing symmetrically at midcell (Brown *et al.*, 2012). Other members of the *Rhizobiales* proliferate by budding, generating new offspring either directly adjacent to the mother cell body (e.g. *Rhodopseudomonas*) or at the tip of a thin stalk-like extension emanating from it (*Hyphomicrobiaceae*) (Whittenbury and McLee, 1967; Whittenbury and Dow, 1977; Moore, 1981; Williams *et al.*, 2016). Unlike the *Rhizobiales*, the *Caulobacterales* possess all typical elongasome components. Consistently, their prototypical member *C. crescentus* displays MreB-dependent dispersed PG incorporation before it switches to FtsZ-mediated zonal growth and cell constriction at midcell (Figge *et al.*, 2004; Gitai *et al.*, 2004). In addition, it features a polar stalk-like extension that is physiologically separated from the cell body (Schlimpert *et al.*, 2012) and synthesized in an elongasome-dependent manner (Wagner *et al.*, 2005). Whereas *C. crescentus* and other members of the *Caulobacteraceae* divide by asymmetric binary fission (Poindexter, 1964), the closely related

Hyphomonadaceae use a budding mechanism phenomenologically similar to that of the *Hyphomicrobiaceae*, in which new offspring emerges from the tip of a stalk structure (Wali *et al.*, 1980; Moore, 1981). Cell division then occurs highly asymmetrically at the bud neck, giving rise to a stalked mother cell and a non-stalked daughter cell. This diversity of morphogenetic programs and enzymatic repertoires suggests significant differences in the mechanisms of polar growth between different bacterial lineages, warranting a closer analysis of the underlying pathways. However, for the stalked budding *Hyphomonadaceae*, achieving this aim has been complicated by the lack of genetically amenable model organisms. This difficulty has been overcome by the recent development of molecular tools for their representative *Hyphomonas neptunium* (Jung *et al.*, 2015), which has opened the door to in-depth studies of the fascinating developmental cycle of this species.

Here, we comprehensively study growth and PG biosynthesis in *H. neptunium*. We show that, unlike suggested previously (Zerfas *et al.*, 1997), the stalk and the nascent bud form a continuum with the mother cell, with bud formation occurring through elongation of the stalk and subsequent remodeling of its terminal region into the new daughter cell compartment. Muropeptide analysis indicates high PG turnover rates and the lack of 3,3-crosslinks, which are thought to be the hallmark of L,D-TPase-mediated polar growth in *A. tumefaciens* (Cameron *et al.*, 2014; Grangeon *et al.*, 2015). To identify the key components of the PG biosynthetic machinery, we comprehensively investigate both the functional significance and localization patterns of predicted PG biosynthetic enzymes and their known regulators. In doing so, we identify several proteins that localize to distinct growth zones and reveal a critical role of the elongasome components MreB and PBP2, but not LDTs, in cell morphogenesis. Based on our results, we postulate that the extraordinary cell shape of *H. neptunium* is achieved by a cell cycle-regulated switch between several distinct sites of dispersed and zonal PG incorporation.

RESULTS

The stalk and bud form a continuum with the mother cell

To gain a better understanding of the morphological transformations that *H. neptunium* undergoes over the course of its life cycle, we analyzed its ultrastructure using electron cryo-tomography. This method allows the three-dimensional imaging of specimens flash-frozen in growth medium without sectioning and staining, thereby preventing preparation artifacts (Gan and Jensen, 2012). Tomographic reconstructions of cells at different developmental stages show that the cytoplasm is bounded by a standard Gram-negative envelope consisting of an inner membrane, a PG layer, and an outer membrane (**Fig. 2**). Its center is occupied by a clearly visible nucleoid, surrounded by large electron-dense ribosomal particles. New-born swarmer cells are shaped asymmetrically, with a round old and a tapered new cell pole (**Fig. 2A;** ratio of round:tapered pole curvature: 0.4 ± 0.1; n = 10; data not shown). Consistent with previous reports (Leifson, 1964; Wali *et al.*, 1980), their old pole carries a single flagellum, which is shed during the early stages of the cell cycle and re-formed at the opposite pole in the nascent swarmer cell compartment (**Fig. 2A, G, and H**). Cells grow slightly in length and round up as they initiate stalk formation by bulging of the envelope at the new pole (**Fig. 2B**; see also **Fig. S1**). The stalk has a uniform diameter of 131 nm (± 3 nm; n = 50) and forms a continuum with the mother cell body. Unlike its *C. crescentus* counterpart (Schlimpert *et al.*, 2012), it features an appreciable cytoplasmic space (60 ± 2 nm diameter; n=50) and is not compartmentalized by crossband-like diffusion barrier complexes (**Fig. 2D**). Importantly, the cytoplasmic membrane consistently lines the stalk envelope and does not invaginate to form chains of pseudo-vesicles, as reported previously (Zerfas *et al.*, 1997), probably based on artifacts arising from chemical fixation and dehydration (Pilhofer *et al.*, 2010). At the onset of bud formation, the tip of the stalk becomes slightly enlarged. The bud then increases in both diameter and length (**Fig. 2E-G**), until it separates from the mother cell by fission at the stalk-bud junction (**Fig. 2H**). Collectively, these data show that the stalk is an integral part of the *H. neptunium* cell that seamlessly connects the mother cell with the nascent bud, likely enabling the free diffusion of small molecules and proteins between these two compartments.

H. neptunium cells are shaped by dynamic changes between dispersed and zonal growth

The electron cryo-tomographic data suggest that the bud forms by gradual expansion of the stalk tip. However, it remained unclear whether it arises *de novo* by addition of new cell material to the end of the stalk or rather through remodeling of the existing stalk structure. To address this issue, we followed the development of single *H. neptunium* cells grown under steady-state conditions in a microfluidic

system (**Fig. 3A** and **Movie S1**). In this experimental setup, swarmer cells took ~ 4 h to differentiate into stalked cells and produce their first offspring (**Fig. 3A**). However, once the stalk was fully established and the first division cycle was completed, new siblings were released at ~2.5 h intervals (**Fig. 3B**). Monitoring cell body, stalk, and bud length over the course of multiple cell cycles, we found that the length of the mother cell body no longer increased after the swarmer-to-stalked cell transition (**Fig. 3B and S1**). Stalk length, by contrast, changed considerably over the course of each cell cycle. At the beginning, it increased to a fixed maximum value. However, once bud formation initiated, the stalk shortened again while the bud was increasing in length (**Fig. 3B**). These results clearly demonstrate that the bud originates from the terminal regions of the stalk structure, which are gradually remodeled to reach the dimensions of the new daughter cell. Notably, previous work has suggested that stalked budding members of the family *Hyphomonadaceae* can produce less than ten offspring before undergoing cell death (Whittenbury and Dow, 1977; Moore, 1981). However, *H. neptunium* cells divided at least 30 times without any noticeable decrease in reproduction rate or obvious morphological defects (data not shown).

To further investigate the mechanism of cell morphogenesis in *H. neptunium*, we localized the sites of active growth at different stages of the cell cycle. To this end, cells were pulse-labeled with the fluorescent D-amino acid hydroxycoumarin-carbonyl-amino-D-alanine (HADA), which can replace D-Ala[4] or D-Ala/Gly[5] in the lipid II peptide side chain and thus become incorporated into PG that is newly synthesized while HADA is available in the medium (Kuru *et al.*, 2012). Fluorescence microscopic analysis of the labeled cells revealed the existence of multiple distinct growth zones (**Fig. 3C**). During the swarmer-to-stalked cell transition, PG was incorporated throughout the cell body, consistent with the general increase in cell size observed during this stage of the cell cycle. The signal then condensed into a bright focus at the new cell pole at the onset of stalk formation, and this pattern persisted until the stalk had reached its maximal length and budding initiated. Thus, as in the related non-budding species *C. crescentus* (Schmidt and Stanier, 1966), the stalk emerges from the cell body through insertion of new material at its base. At the onset of bud formation, the signal was transiently spread throughout the stalk and then gradually condensed in the nascent bud compartment. Later in the cell cycle, PG synthesis was limited almost exclusively to the bud, with an additional focus appearing at the division site before its final separation, likely reflecting the remodeling of PG at the division site. The same succession of PG insertion patterns is apparent from a quantitative analysis of the HADA signals in populations of swarmer, stalked and budding cells (**Fig. 3D**). These data indicate that the morphology of *H. neptunium*

is determined by a complex cell cycle-regulated pattern of PG biosynthesis that involves the establishment of several distinct zones of dispersed and zonal growth.

The cell wall of *H. neptunium* shows distinctive compositional features

Previous studies have suggested that the polar growth of *A. tumefaciens* depends on the activity of L,D-TPases (Cameron *et al.*, 2014; Grangeon *et al.*, 2015), consistent with the unusually high content of 3,3-crosslinks (> 50%) observed in the PG of this species (Brown *et al.*, 2012). Other unusual features of *A. tumefaciens* that may be related to its peculiar mode of growth include a high degree of total cross-linking (~ 64%) and the lack of 1,6-anhydro muropeptides, which may point to the presence of unusually long glycan backbones (> 250 disaccarides/chain) (Brown *et al.*, 2012). To clarify whether similar mechanisms may be at work in stalked budding bacteria, we determined the muropeptide profile of PG from growing *H. neptunium* cells, using a highly sensitive method based on UPLC and in-line detection of the PG fragments by electrospray mass spectrometry (**Fig. 4** and **Table 1**). In parallel, we performed an analysis of PG from *C. crescentus*, whose results were comparable to those of a previous study (Takacs *et al.*, 2013), thus validating our methodological approach. In both cases, about 72% of the muropeptides detected could be identified, including all major species. Importantly, *H. neptunium* cell walls lacked 3,3-linked muropeptides and showed only a relatively low degree of crosslinking (22%). On the other hand, they contained a significant fraction of 1,6-anhydro muropeptides (9.6%), indicating an average glycan chain length of only 11 disaccharide units. Notably, more than 90% of all peptide side chains were tetrapeptides. Together with the low degree of crosslinking, this finding may indicate a high rate of PG turnover and/or significant levels of carboxypeptidase activity. We further found that in *H. neptunium* cell walls, pentapeptide side chains exclusively contained glycine instead of D-alanine at their fifth position. While glycine can also replace D-Ala^5 in a fraction of the pentapeptides in *C. crescentus* when supplied in the growth medium (Takacs *et al.*, 2013) (**Fig. 4**), this modification is not detectable in *A. tumefaciens* and its relatives (Brown *et al.*, 2012). Collectively, our data reveal fundamental differences in the composition of *H. neptunium* and *A. tumefaciens* cell walls, suggesting that these two species use distinct sets of enzymes to achieve asymmetric growth. In contrast, and consistent with their close phylogenetic relationship, *H. neptunium* and *C. crescentus* share a comparable cell wall composition (**Table 1**) and may thus use similar PG biosynthetic machineries for growth.

***H. neptunium* cell shape is influenced by a redundant set of PG hydrolases**

The low abundance of pentapeptide side chains suggests an important role of PG hydrolases in *H. neptunium* cell wall biogenesis. To identify key players in the lytic machinery, we performed a comprehensive mutational analysis of all predicted hydrolase genes identified in the *H. neptunium* genome (**Table S1**). Moreover, we determined the localization patterns of the corresponding gene products to identify factors that specifically localized to the different growth zones identified by HADA labeling.

Initially, we focused on putative endopeptidases of the LytM family, characterized by an M23 metallopeptidase domain. Members of this group were shown to act as PG-processing enzymes in other species. In addition, there are catalytically inactive variants that have adopted a regulatory role in the activation of divisome-associated PG hydrolases involved in cell constriction or separation (Uehara and Bernhardt, 2011). The six family members encoded in the *H. neptunium* genome, named LmdA-F (LytM domain-containing protein A-F), display the typical structure of LytM homologs, with a non-structured or coiled-coil-containing N-terminal region and a C-terminal M23 peptidase domain (**Fig. 5A**). It was possible to generate in-frame deletions in all of the corresponding ORFs except for *lmdC*, suggesting that this gene may be essential. Among the strains obtained, only the *lmdE* mutant showed an obvious phenotype, forming elongated stalks that are associated with short chains of bud cells (**Fig. 5B, 5C, and S2**). Interestingly, LmdE lacks several conserved catalytic residues in its M23 peptidase domain (data not shown). Consistent with the chaining phenotype observed for the deletion strain, it may therefore also act as a regulatory factor with a role in cell division. To determine whether LmdE or its paralogs were recruited to the division site or any other growth zone of *H. neptunium*, we fused the proteins with a C-terminal red fluorescent protein (mCherry) tag using allelic exchange. In several cases, the full-length fusion protein was undetectable by Western blot analysis due to cleavage of the fluorescent tag, preventing further analysis. The stable constructs (fusions to LmdA, LmdB, and LmdD) showed only diffuse periplasmic fluorescence, suggesting that they do not stably interact with the major PG biosynthetic complexes (data not shown).

The low pentapeptide content of *H. neptunium* cell walls may, at least in part, reflect the action of D-Ala-D-Ala carboxypeptidases, which remove the terminal, fifth amino acid from the peptide side chains (Höltje, 1998). Based on their characteristic S13 or β-lac_2 domains (**Fig. 5A**), we identified three potential members of this enzyme family in *H. neptunium,* now called DacB, DacL, and DacH (D-alanine-D-alanine carboxypeptidase B-H). DacB is a close homolog of DacB from *E. coli* (Korat *et al.*, 1991), whereas DacH and DacL are specific for *H. neptunium* and its relatives. After generating in-frame

deletions in each of the respective genes, only the Δ*dacB* mutant showed obvious morphological defects, as reflected by a mild stalk elongation and chaining phenotype (**Fig. 5B, 5C, and S2**). However, only DacL turned out to have a distinct localization pattern and condensed into a focus at the new pole during the onset of stalk formation (**Fig. 5D, 5F, and S3**), although the functionality of the fusion construct remains to be verified. Individual carboxypeptidases thus appear to make different, but overall only minor contributions to growth and morphogenesis in *H. neptunium* (see also **Fig. S4**).

Another prominent feature of *H. neptunium* cell walls is their high content of 1,6-anhydro muropeptides, which arise from cleavage of the glycan backbone by lytic transglycosylases (Höltje *et al.*, 1975). Searching for proteins with domains typically associated with these proteins, we identified in *H. neptunium* two putative membrane-bound lytic transglycosylases (MltA and MltB), a homolog of the rare lipoprotein A (RlpA), and a predicted soluble lytic transglycosylase (SltA). In addition, we found a glycoside hydrolase with predicted lysozyme activity (GplA), which was also included in our analysis (**Fig. 5A**). The majority of strains with in-frame deletions in the respective genes displayed wild-type morphology. The only exception was the *⊿mltA* mutant, which occasionally formed short chains of buds, suggesting a role of MltA in cell division (**Fig. 5B, 5C, and S2**). Localization studies were only possible for SltA, because fluorescently tagged derivatives of the other proteins were unstable and barely detectable by Western blot analysis. SltA-mCherry showed a diffuse distribution pattern, again suggesting that its enzymatic activity is not controlled at the level of protein localization (data not shown).

A fourth group of PG hydrolases important for cell growth are the N-acetylmuramyl-L-alanine amidases, which include Ami_3 and CHAP domain-containing proteins. Analysis of the *H. neptunium* genome revealed only a single amidase homolog, now called AmiC, which is predicted to be a membrane-attached protein containing a periplasmic Ami_3 domain (**Fig. 5A**). Deletion of *amiC* led to the formation of elongated stalks terminated by chains of bud cells, suggesting a role for the protein in the final stages of cell division (**Fig. 5B and 5C**). Localization studies indeed showed that an inducible, fully functional (data not shown) AmiC-fusion localized to the division site during late stages of the cell cycle. After cytokinesis, it remained associated with the new pole until the daughter cell entered the next division cycle and initiated stalk formation (**Fig. 5E, 5F, and S3**). However, an additional function of AmiC in stalk growth is unlikely, given the long-stalk phenotype of the deletion mutant.

Collectively, our mutational and localization studies indicate that most of the predicted PG hydrolases of *H. neptunium* are redundant and not required for proper development under laboratory conditions.

Consistent with this observation, all deletion mutants analyzed showed normal doubling times in growth experiments (**Fig. S4**). The only hydrolases with critical roles are LmdC, which may be essential, as well as LmdE and AmiC, which both appear to be required for efficient release of the mature bud from the mother cell.

D,D-TPases and bifunctional PBPs play a key role in *H. neptunium* growth

In the established model systems, growth processes such as cell elongation and division are to a large extent determined by the localization and/or activation of PG synthases. The genome of *H. neptunium* encodes three predicted bifunctional PBPs (now called PBP1A, PBP1X, and PBP1C), two monofunctional D,D-TPases (PBP2, PBP3), and one monofunctional GTase (MtgA) (Derouaux *et al.*, 2008). In addition, it contains two ORFs coding for proteins with putative LDT activity (now called LdtA and LdtB), as suggested by their LD_TP (YkuD) domain (**Fig. 6A and Table S1**). To address the function of these factors, we set out to generate strains carrying in-frame deletions in each of the respective genes. It was not possible to obtain mutants lacking PBP1A, PBP2, or PBP3, suggesting that these PG synthases may be essential for viability (data not shown). The two remaining PBPs, by contrast, appeared to be dispensable. Deletion of *pbp1X* led to excessive stalk elongation and increased bud size, as is typical for strains with cell division defects (unpublished data). Mutation of *pbp1C*, by contrast, did not produce any obvious phenotype nor did it aggravate the defects of the Δ*pbp1X* mutant (**Fig. 6B and 6C**). Similar to its *E. coli* homolog (Schiffer and Höltje, 1999), PBP1C may therefore not contribute significantly to PG synthesis under standard conditions.

Previous studies have suggested that LDTs play a major role in the polar growth of *A. tumefaciens*, because they localize to the tip of the nascent daughter cell (Cameron *et al.*, 2014; Grangeon *et al.*, 2015) and mediate the formation of 3,3-crosslinks, which make up more than 50% of all peptide cross-links in this species (Brown *et al.*, 2012). However, it was possible to delete *ldtA*, *ldtB*, or both genes in *H. neptunium* without significantly affecting cell morphology (**Fig. 6C and S5A**) or growth rates (**Fig. S5B**). Consistent with the absence of 3,3-linked muropeptides (**Fig. 4** and **Table 1**), this class of PG synthases thus appears to be largely dispensable for PG synthesis and proper development in *H. neptunium* under standard growth conditions. Similarly, MtgA may only have a redundant function because its inactivation had no obvious phenotypic consequences (**Fig. 6C, S5A and S5B**).

Collectively, our mutational analyses suggest that generic mono- and bifunctional PBPs may be key factors in *H. neptunium* growth. To further clarify the functions of these proteins, we set out to generate fluorescent protein fusions by replacing their native genes with alleles encoding fluorescently tagged

derivatives. Localization studies of the bifunctional PBPs were again complicated by the fact that, in several cases, the fusion proteins were quantitatively cleaved, although similar constructs were successfully used to localize bifunctional PBPs in *C. crescentus* (Strobel *et al.*, 2014). The only stable construct obtained was YFP-PBP1A. It was able to functionally replace the wild-type protein and evenly distributed within the cells (data not shown). Strains producing Venus-PBP2 and Venus-PBP3 were also readily obtained and did not show any defects in cell morphology (**Fig. S3**) or growth rate (data not shown). Microscopic analysis revealed that Venus-PBP2 had a diffuse or patchy pattern in swarmer cells but then condensed at the stalked pole at the onset of stalk formation. Once a visible bud had formed, this polar complex disappeared, and the fusion was detected in multiple faint patches scattered within the mother cell, the stalk, and the bud (**Fig. 6D and 6F**). These findings suggest that PBP2 and other elongasome components may contribute to all aspects of *H. neptunium* growth. In contrast, Venus-PBP3 predominantly localized to the division site of late budding cells. The fusion remained briefly associated with the new pole but then dispersed evenly within the cell once a visible stalk was formed (**Fig. 6E, 6F, and S6**). As in other bacteria, PBP3 thus appears to be an integral part of the divisome specifically involved in septal cell wall remodeling. Consistent with this notion, it colocalizes with FtsZ at the future division site during the late stages of cell division (unpublished data).

The elongasome components MreB and RodZ localize to the sites of PG synthesis

The patchy distribution of PBP2 was reminiscent of the pattern observed for MreB and other elongasome components in previously studied bacteria (Typas *et al.*, 2012). Moreover, we were not able to generate a mutant carrying an in-frame deletion in the *mreB* gene (data not shown), suggesting that similar to PBP2, MreB may be essential in *H. neptunium*. This would be in strong contrast to the situation observed for *A. tumefaciens*, which lacks MreB and achieves polar growth without any of the elongasome components. To visualize MreB, we generated a strain in which the native *mreB* gene was replaced by an allele encoding an MreB-mCherry^{SW} sandwich fusion, ensuring a native expression pattern. In this construct, the fluorescent protein tag was integrated into a loop that is exposed at the surface of the MreB molecule (**Fig. 7A**), as previously reported for the *E. coli* homolog (Bendezu *et al.*, 2009). The resulting strain was viable and showed no significant morphological defects (**Fig. S3A**). Microscopic analysis indicated that the fusion protein showed a localization pattern reminiscent of that of Venus-PBP2 (**Fig. 7B and 7C**). Whereas most swarmer cells showed a diffuse or patchy signal, MreB-mCherry^{SW} partly condensed at the future stalked pole during early stages of the cell cycle. This pattern was maintained until the stalk had formed and budding initiated. In early budding cells, patchy fluorescence was detected in all parts of the cell, including the stalk, whereas these signals were later

largely confined to the mother and bud cell compartments (**Fig. 7B and 7C**). MreB thus localizes to the main growth zones of *H. neptunium* (compare **Fig. 3C**), suggesting that it could be an important player in stalk formation and budding. Notably, its recruitment to the mother cell body suggests that peptidoglycan is still turned over in this part of the cell, even though its overall dimensions remain largely constant once formation of the first bud has initiated (**Fig. S1**). This notion is consistent with the observation of weak but significant HADA labeling in the mother cell compartment throughout later stages of the cell cycle (**Fig. 3C**).

To determine whether the distribution pattern of MreB reflected that of other elongasome components, we additionally analyzed the localization of RodZ, using a fully functional YFP-RodZ fusion (**Fig. S3**). The pattern obtained was indeed very similar to that observed for MreB (**Fig. 7D and 7E**), supporting the idea that MreB-directed elongasome activity may be critical for *H. neptunium* development.

Inhibition of MreB leads to severe morphological defects

Both our inability to delete *mreB* and the localization of MreB and RodZ to the zones of active growth indicate a role of the elongasome in *H. neptunium* stalk and bud formation. To further support this hypothesis, we analyzed the effects caused by inhibition of MreB function with the small molecule MP265 (Takacs *et al.*, 2010). This compound was shown to bind close to the nucleotide-binding pocket of MreB in *C. crescentus* and other species, thereby preventing its proper polymerization (Bean *et al.*, 2009; van den Ent *et al.*, 2014). Given the predicted high similarity of *H. neptunium* MreB to its homolog from *C. crescentus* (**Fig. S7**), the effect of the inhibitor was likely to be conserved. Growth experiments indeed showed that its addition to the culture medium led to a concentration-dependent decrease in the growth rate (**Fig. 8A**). At the same time, treatment with MP265 significantly changed cell morphology (**Fig. 8B-D**). At low concentrations (5 µM), it mostly affected cell length, leading to the accumulation of stalked cells with unusually long cell bodies as well as budding cells connected by highly elongated stalks (data not shown). Higher concentrations, by contrast, induced a considerable increase in both length and width of the cell bodies. In addition, they caused the formation of stubby and/or abnormally thick stalks (**Fig. 8B**), reminiscent of the defects observed for MreB-depleted *C. crescentus* cells (Wagner *et al.*, 2005). These effects were reversible, because cells quickly resumed growth and regained wild-type morphology once MP265 was removed from the medium (**Fig. 8B**). Similar effects were also observed after treatment of cells with the structurally similar inhibitor A22 (Iwai *et al.*, 2002) (**Fig. S8A-D**). Notably, previous work has shown that MP265 and A22 not only affect MreB but also other cellular targets, as they can impair the growth of species lacking actin homologs (including *A. tumefaciens*) when

added at elevated concentrations. However, this non-specific growth inhibition is not accompanied by changes in cell morphology (Takacs *et al.*, 2010), indicating that the cell shape defects observed for *H. neptunium* indeed result from the impairment of MreB function. Consistent with this idea, addition of MP265 or A22 led to the delocalization of MreB-mCherry^{SW} (**Fig. S8E**) and to a concomitant loss of localized PG biosynthesis (**Fig. S9**). Collectively, these results strongly suggest that proper elongasome function is critical for normal development in *H. neptunium*.

DISCUSSION

This work is the first molecular study of growth and development in *H. neptunium* and stalked budding bacteria in general. Our data reveal that *H. neptunium* cells display a complex cell-cycle regulated pattern of PG incorporation (**Fig. 9**). After an initial general increase in cell size through dispersed PG incorporation, an extended period of zonal growth at the new cell pole leads to extrusion of the stalk structure. This mode of stalk elongation is similar to that observed in other stalked alphaproteobacteria such as *C. crescentus* (Aaron *et al.*, 2007), suggesting conservation of the underlying machinery. At the onset of bud formation, however, the cell establishes a new zone of localized dispersed growth at the tip of the stalk, thereby remodeling the terminal stalk region into a new daughter cell compartment. Finally, cytokinesis is mediated by a second, short phase of zonal growth at the bud neck. This pattern of PG biosynthesis is very different from that observed during polar growth in *A. tumefaciens* and its relatives. In these species, formation of the new cell half is mediated by tip extension, i.e. the continuous addition of new cell wall material in the polar region of the cell (**Fig. 9**). At the onset of cell division, cell wall biosynthesis then switches toward midcell to drive cell constriction and then remains associated with the new cell poles, mediating the next round of cell elongation (Brown *et al.*, 2012; Cameron *et al.*, 2014). Thus, despite their evolutionary closeness, alphaproteobacteria appear to have evolved different mechanisms to achieve asymmetric growth.

The distinct growth modes of *H. neptunium* and *A. tumefaciens* are also reflected by their distinctive cell wall architectures. The two species show considerable differences in the average length of the PG glycan strands and the degree of crosslinking. Moreover, *H. neptunium* completely lacks 3,3-crosslinks, whereas this type of connection is highly abundant in *A. tumefaciens* (Brown *et al.*, 2012). This observation is consistent with the fact that LDTs, i.e. the enzymes generating 3,3-crosslinks, are dispensable for proper development in *H. neptunium*, whereas they are thought to be key mediators of polar growth in the Rhizobiales (Cameron *et al.*, 2014; Grangeon *et al.*, 2015). The unusual cell wall composition and importance of LDTs in the *Rhizobiales* is in line with the apparent loss of MreB and other elongasome-specific proteins in this alphaproteobacterial order. *H. neptunium*, by contrast, possesses a typical elongasome, which is consistently localized to the zones of active PG incorporation and critical for proper cell morphology and growth. The *Hyphomonadaceae* thus appear to use a similar PG biosynthetic machinery as the related, stalked but non-budding *Caulobacteraceae*, but they must have evolved novel mechanisms to control the activity of this machinery and thus expand their repertoire of

growth modes. Unraveling the nature of these mechanisms will provide important new insights into the molecular principles that govern morphogenesis in bacterial cells.

Apart from the features mentioned above, the *H. neptunium* cell wall is characterized by a very low content of pentapeptide side chains, which suggests a high rate of PG turnover or processing. Interestingly, the pentapeptides detected exclusively contained glycine at their 5th position. The function of this modification still remains to be determined. It is conceivable that Gly^5-containing pentapeptides are poorer TPase substrates than their D-Ala^5-containing derivatives and thus accumulate in the cell, serving as a means to control the degree of PG crosslinking. However, given the complete absence of D-Ala^5-containing pentapeptides in our analysis, it is unclear whether this species is simply turned over so rapidly that it does not accumulate to detectable levels or whether it is not synthesized at all. It also remains to be determined whether Gly^5-modified pentapeptides are limited to distinct growth zones to differentially regulate PG biosynthesis within the *H. neptunium* cell.

Our analysis of the PG biosynthetic machinery in *H. neptunium* revealed only a small set of essential PG synthases, including PBP2, PBP3 and PBP1A. Based on the results of localization studies, we suggest that, as in *E. coli* and other bacteria (Spratt, 1975; Typas *et al.*, 2012), PBP2 is responsible for dispersed PG incorporation, whereas PBP3 is specifically involved in cell division. PBP1A may participate in both of these processes, because bifunctional PBPs critically contribute to elongasome as well as divisome function (Typas *et al.*, 2012) and *H. neptunium* cells are viable in the absence of the non-essential paralogs PBP1X and PBP1C. Nevertheless, PBP1X may be the preferred choice for cell division, because mutants lacking this protein show defects that indicate delay in cytokinesis. In contrast, a high degree of redundancy was observed for the PG hydrolases of *H. neptunium*. With the exception of LmdC, whose function is still unclear, all other proteins investigated were dispensable for growth. The strongest phenotypes were observed for strains deficient in the amidase AmiC or the atypical M23 domain-containing protein LmdE, whose absence again caused a defect in the final steps of cell division. This situation is similar to that in *E. coli*, where the amidases AmiABC and their M23-domain-containing regulators EnvC and NlpD are required for efficient cleavage of the division septum (Heidrich *et al.*, 2001; Uehara *et al.*, 2010). Given that many of the PG hydrolase families identified in *H. neptunium* are represented by several different proteins, it is possible that these factors have overlapping or redundant functions. An important aim for the future will be to unravel the mechanisms that spatiotemporally control the activity of the PG synthases and hydrolases in *H. neptunium* to mediate several distinct modes of growth in a single bacterial cell.

Collectively, the *Hyphomonadaceae* are an intriguing group of organisms whose study is bound to shed new light on the biology of bacteria. Our work indicates that the members of this family have evolved a unique mode of growth that involves the establishment of multiple zones of dispersed and zonal cell peptidoglycan incorporation. It will be interesting to dissect the mechanisms controlling bud formation and asymmetric cell division at the bud neck. Another important question concerns the coordination of morphological development with other cell cycle-regulated processes such as chromosome segregation and flagellar placement. Addressing these issues will help to unravel the mechanisms underlying the striking morphological diversity of alphaproteobacteria and the selective advantages provided by their different developmental cycles.

EXPERIMENTAL PROCEDURES

Bacterial strains and growth conditions. All *H. neptunium* strains used in this study were derived from the wild type LE670 (ATCC 15444) (Leifson, 1964). Cells were cultivated aerobically in MB medium (Difco Marine Broth 2216; BD Biosciences) at 28 °C in baffled flasks with shaking at 210 rpm. Media were supplemented with kanamycin (100/200) or sucrose (-/3%) when appropriate (µg/ml in liquid/solid medium). *C. crescentus* NA1000 (Evinger and Agabian, 1977) was grown in peptone-yeast extract (PYE) medium at 28 °C with shaking at 210 rpm. *E. coli* strains were grown in LB Medium (Carl Roth) at 37 °C, and media were supplemented with kanamycin (30/50) (µg/ml in liquid/solid media). *E. coli* WM3064 was cultivated in the presence of 300 µM 2,6-diaminopimelic acid (DAP). *E. coli* TOP10 (Invitrogen) was used for cloning purposes. To record growth curves, cells were cultivated at 28 °C and 205 rpm in 24-well polystyrene microtiter plates (Becton Dickinson Labware) and the cell densities (OD_{580}) were measured at 15 min intervals with a Tecan Infinity M200Pro microplate reader.

Construction of plasmids and bacterial strains. The strains, plasmids, and oligonucleotides used in this study are detailed in **Tables S2-S6**. *H. neptunium* was transformed by conjugation as described previously (Jung *et al.*, 2015). Chromosomal in-frame deletions were generated by double-homologous recombination, using *sacB*-containing suicide vectors and a two-step procedure based on sucrose counterselection (Thanbichler and Shapiro, 2006). For this purpose, *H. neptunium* cells were transformed with non-replicating plasmids containing the flanking regions and the terminal 8-12 codons of the genes to be deleted. After verification by colony PCR, transformants were grown to stationary phase (for 24 h) in MB medium. 200 µL of a 1:200 dilution were plated on MB agar containing 3% sucrose, which were incubated at 28 °C until colonies appeared (5-7 days). Individual colonies were restreaked in parallel onto MB agar supplemented with sucrose or kanamycin, respectively. After 48 h of growth, clones growing on sucrose-containing but not on kanamycin-containing media were tested for deletion of the gene of interest by colony PCR. At least 100 clones originating from four different single-recombinants were analyzed to conclude on the potential essentiality of a gene. The same method was used for the replacement of chromosomal genes with alleles encoding fluorescent protein fusions.

Microscopy. Cultures were grown to exponential phase in MB medium and, if suitable, induced with 300 µM $CuSO_4$ or treated with growth inhibitors as indicated. Cells were transferred onto 1% agarose pads and analyzed with a Zeiss Axio Observer.Z1 microscope (Zeiss, Germany) equipped with a Zeiss Plan-Apochromat 100x/1.46 Oil DIC M27 objective, Chroma ET-YFP and ET-mCherry filter sets, and a pco.edge sCMOS camera (PCO, Germany). Images were processed with Metamorph 7.7.5 (Universal

Imaging Group, USA), Photoshop CS2, and Illustrator CS5 (Adobe Systems, USA). Microfluidic experiments were performed using B04A microfluidic plates (Millipore) with a F84 manifold coupled to an ONIX EV262 Microfluidic System (CellASIC, USA). To this end, exponentially growing cells were flushed into the flow cell, cultivated under continuous medium flow (0.4 µl/h), and imaged at regular intervals using the set-up described above.

Electron cryo-tomography. *H. neptunium* cells were grown in MB medium to an OD_{600} of 0.5 and mixed with 10 nm colloidal gold (Sigma-Aldrich, St. Louis, MO) pretreated with bovine serum albumin, which served as fiducial marker during tomogram reconstruction. 3 µl of the resulting sample were pipetted onto a freshly glow-discharged Quantifoil copper R2/2 200 EM grid (Quantifoil Micro Tools GmbH, Jena, Germany) and plunge-frozen in a liquid ethane-propane mixture (Tivol *et al.*, 2008) using an FEI Vitrobot mark-III (FEI Company, Hillsboro, OR). The frozen grid was then imaged in an FEI Tecnai G2 Polara 300 keV field emission transmission electron microscope (FEI Company, Hillsboro, OR) equipped with a Gatan energy filter (Gatan, Pleasanton, CA) and a Gatan UltraCam detector (Gatan, Pleasanton, CA). Energy-filtered tilt series of images of the cells were collected automatically from −64° to +64° at 1° intervals using the UCSF Tomography data collection software (Zheng *et al.*, 2007) with a total dosage of 150 $e^-/Å^2$, a defocus of -10 µm, and a pixel size of 3.9 Å. The images were aligned and subsequently reconstructed into tomograms by the weighted back-projection method using the IMOD software package (Kremer *et al.*, 1996).

Peptidoglycan labeling. 250 µL of a mid-exponentially growing *H. neptunium* culture were mixed with 1.25 µL 100 mM hydroxycoumarin-carbonyl-amino-D-alanine (HADA) (Kuru *et al.*, 2012) and incubated with shaking at 180 rpm for 9 min at 28 °C. After addition of ice-cold ethanol to a final concentration of 35%, the suspension was incubated for 10 min on ice in the dark. The cells were harvested by centrifugation for 2 min at 9,000 rpm, washed three times with PBS (137 mM NaCl, 2.7 mM KCl, 10 mM Na_2HPO_4, 2 mM KH_2PO_4), and finally resuspended in 100 µL PBS prior to imaging.

Peptidoglycan analysis. To determine the muropeptide profile of *H. neptunium* LE670 and *C. crescentus* NA1000 (Evinger and Agabian, 1977), cells were grown in 250 mL MB or PYE medium, respectively, to an OD_{600} of 0.7. They were harvested for 10 min at 7,000 x g and 4 °C, resuspended in 1 mL de-ionized H_2O, and heated for 10 min at 100 °C. Cell lysates were snap-frozen in liquid nitrogen, lyophilized, and analyzed essentially as described previously (de Jonge *et al.*, 1992) (ANASYN, Germany). In short, PG was isolated from 10 mg of lyophilized cells and digested with mutanolysin. After reduction with sodium borohydrate, muropeptides were separated on a C18 reversed-phase column by ultra-performance

liquid chromatography (UPLC) using a linear gradient of 0-30% methanol in 0.1% trifluoroacetic acid and identified by mass spectrometry.

Bioinformatic analyses. All DNA and protein sequences were retrieved from the GenBank database (Benson *et al.*, 2014) at the National Center for Biotechnoloy Information (NCBI). The domain structure of proteins was obtained from the Pfam database (Finn *et al.*, 2014). The secondary structure of proteins was predicted using the PSIPRED server (http://bioinf.cs.ucl.ac.uk/psipred) (Buchan *et al.*, 2013), whereas 3D structural models were calculated with the iTasser server (Yang *et al.*, 2015). Imaging data were analyzed with MetaMorph 7.7.0.0 (Universal Imaging Group) or Fiji 1.41K (Schindelin *et al.*, 2012). Box plots were created with QtiPlot 0.9.8.7 (IONDEV SRL, Romania). Demographs were generated in R version 3.1.1 (Team, 2012) using the Cell Profiles script (http://github.com/ta-cameron/Cell-Profiles) (Cameron *et al.*, 2014). Phylogenetic analysis was performed with ClustalX2 (Larkin *et al.*, 2007), using the neighbor-joining method and bootstrapping (100 trials) to provide statistical support for nodes. The accession numbers of the GyrA homologs used are WP_054361461.1, WP_047308558.1, ADP72527.1, WP_013216135.1, AIJ54459.1, AEH79268.1, CDN90892.1, ADU14736.1, YP_002517024.1, ABI76923.1, ACT59110.1, EBA09010.1, WP_025062085.1, EAP76397.1, and NP_416734.1.

ACKNOWLEDGEMENTS

We thank Erkin Kuru and Yves Brun for advice on the use and synthesis of HADA, Julia Rosum for excellent technical assistance, and Wolfgang Strobel for support in the initial phases of this work. Moreover, we are grateful to Daniela Kiekebusch, Maria Billini, and Alexandra Jung for critical reading of the manuscript. M.T. acknowledges core support from Philipps-Universität Marburg, funding from the German Research Foundation (DFG) through Research Training Group (GRK) 1216, and a Max Planck Fellowship from the Max Planck Society. Work in the laboratory of G.J.J. is supported by the Howard Hughes Medical Institute.

AUTHORS' CONTRIBUTIONS

EC, SR, SE, and CR performed the genetic and cell biological analyses. YC, JS, and GJJ conducted the electron cryo-tomography studies. LS and UK carried out the synthesis of HADA. MT designed the study. EC and MT wrote the paper, with input from all other authors.

CONFLICT OF INTEREST STATEMENT

The authors have no conflicts of interest related to this work.

REFERENCES

Aaron, M., Charbon, G., Lam, H., Schwarz, H., Vollmer, W., and Jacobs-Wagner, C. (2007) The tubulin homologue FtsZ contributes to cell elongation by guiding cell wall precursor synthesis in *Caulobacter crescentus*. *Mol Microbiol* **64**: 938-952.

Alyahya, S.A., Alexander, R., Costa, T., Henriques, A.O., Emonet, T., and Jacobs-Wagner, C. (2009) RodZ, a component of the bacterial core morphogenic apparatus. *Proc Natl Acad Sci U S A* **106**: 1239-1244.

Bean, G.J., Flickinger, S.T., Westler, W.M., McCully, M.E., Sept, D., Weibel, D.B., and Amann, K.J. (2009) A22 disrupts the bacterial actin cytoskeleton by directly binding and inducing a low-affinity state in MreB. *Biochemistry* **48**: 4852-4857.

Bendezu, F.O., Hale, C.A., Bernhardt, T.G., and de Boer, P.A. (2009) RodZ (YfgA) is required for proper assembly of the MreB actin cytoskeleton and cell shape in *E. coli*. *EMBO J* **28**: 193-204.

Benson, D.A., Clark, K., Karsch-Mizrachi, I., Lipman, D.J., Ostell, J., and Sayers, E.W. (2014) GenBank. *Nucleic Acids Res* **42**: D32-37.

Bouhss, A., Trunkfield, A.E., Bugg, T.D., and Mengin-Lecreulx, D. (2008) The biosynthesis of peptidoglycan lipid-linked intermediates. *FEMS Microbiol Rev* **32**: 208-233.

Brown, P.J., de Pedro, M.A., Kysela, D.T., Van der Henst, C., Kim, J., De Bolle, X., Fuqua, C., and Brun, Y.V. (2012) Polar growth in the alphaproteobacterial order Rhizobiales. *Proc Natl Acad Sci U S A* **109**: 1697-1701.

Buchan, D.W., Minneci, F., Nugent, T.C., Bryson, K., and Jones, D.T. (2013) Scalable web services for the PSIPRED protein analysis workbench. *Nucleic Acids Res* **41**: W349-357.

Cameron, T.A., Anderson-Furgeson, J., Zupan, J.R., Zik, J.J., and Zambryski, P.C. (2014) Peptidoglycan synthesis machinery in *Agrobacterium tumefaciens* during unipolar growth and cell division. *mBio* **5**: e01219-01214.

Cameron, T.A., Zupan, J.R., and Zambryski, P.C. (2015) The essential features and modes of bacterial polar growth. *Trends Microbiol* **23**: 347-353.

Daniel, R.A., and Errington, J. (2003) Control of cell morphogenesis in bacteria: two distinct ways to make a rod-shaped cell. *Cell* **113**: 767-776.

de Jonge, B.L., Chang, Y.S., Gage, D., and Tomasz, A. (1992) Peptidoglycan composition of a highly methicillin-resistant *Staphylococcus aureus* strain. The role of penicillin binding protein 2A. *J Biol Chem* **267**: 11248-11254.

Derouaux, A., Wolf, B., Fraipont, C., Breukink, E., Nguyen-Disteche, M., and Terrak, M. (2008) The monofunctional glycosyltransferase of *Escherichia coli* localizes to the cell division site and interacts with penicillin-binding protein 3, FtsW, and FtsN. *J Bacteriol* **190**: 1831-1834.

Dominguez-Escobar, J., Chastanet, A., Crevenna, A.H., Fromion, V., Wedlich-Söldner, R., and Carballido-Lopez, R. (2011) Processive movement of MreB-associated cell wall biosynthetic complexes in bacteria. *Science* **333**: 225-228.

Evinger, M., and Agabian, N. (1977) Envelope-associated nucleoid from *Caulobacter crescentus* stalked and swarmer cells. *J Bacteriol* **132**: 294-301.

Fenton, A.K., and Gerdes, K. (2013) Direct interaction of FtsZ and MreB is required for septum synthesis and cell division in *Escherichia coli*. *EMBO J* **32**: 1953-1965.

Figge, R.M., Divakaruni, A.V., and Gober, J.W. (2004) MreB, the cell shape-determining bacterial actin homologue, co-ordinates cell wall morphogenesis in *Caulobacter crescentus*. *Mol Microbiol* **51**: 1321-1332.

Finn, R.D., Bateman, A., Clements, J., Coggill, P., Eberhardt, R.Y., Eddy, S.R., Heger, A., Hetherington, K., Holm, L., Mistry, J., Sonnhammer, E.L., Tate, J., and Punta, M. (2014) Pfam: the protein families database. *Nucleic Acids Res* **42**: D222-230.

Flärdh, K. (2003) Essential role of DivIVA in polar growth and morphogenesis in *Streptomyces coelicolor* A3(2). *Mol Microbiol* **49**: 1523-1536.

Gan, L., and Jensen, G.J. (2012) Electron tomography of cells. *Q Rev Biophys* **45**: 27-56.

Garner, E.C., Bernard, R., Wang, W., Zhuang, X., Rudner, D.Z., and Mitchison, T. (2011) Coupled, circumferential motions of the cell wall synthesis machinery and MreB filaments in *B. subtilis*. *Science* **333**: 222-225.

Gitai, Z., Dye, N., and Shapiro, L. (2004) An actin-like gene can determine cell polarity in bacteria. *Proc Natl Acad Sci U S A* **101**: 8643-8648.

Glauner, B., Holtje, J.V., and Schwarz, U. (1988) The composition of the murein of *Escherichia coli*. *J Biol Chem* **263**: 10088-10095.

Grangeon, R., Zupan, J.R., Anderson-Furgeson, J., and Zambryski, P.C. (2015) PopZ identifies the new pole, and PodJ identifies the old pole during polar growth in *Agrobacterium tumefaciens*. *Proc Natl Acad Sci U S A* **112**: 11666-11671.

Heidrich, C., Templin, M.F., Ursinus, A., Merdanovic, M., Berger, J., Schwarz, H., de Pedro, M.A., and Holtje, J.V. (2001) Involvement of N-acetylmuramyl-L-alanine amidases in cell separation and antibiotic-induced autolysis of *Escherichia coli*. *Mol Microbiol* **41**: 167-178.

Höltje, J.V. (1995) From growth to autolysis: the murein hydrolases in *Escherichia coli*. *Arch Microbiol* **164**: 243-254.

Höltje, J.V. (1998) Growth of the stress-bearing and shape-maintaining murein sacculus of *Escherichia coli*. *Microbiol Mol Biol Rev* **62**: 181-203.

Höltje, J.V., Mirelman, D., Sharon, N., and Schwarz, U. (1975) Novel type of murein transglycosylase in *Escherichia coli*. *J Bacteriol* **124**: 1067-1076.

Iwai, N., Nagai, K., and Wachi, M. (2002) Novel S-benzylisothiourea compound that induces spherical cells in *Escherichia coli* probably by acting on a rod-shape-determining protein(s) other than penicillin-binding protein 2. *Biosci Biotechnol Biochem* **66**: 2658-2662.

Jones, L.J., Carballido-Lopez, R., and Errington, J. (2001) Control of cell shape in bacteria: helical, actin-like filaments in *Bacillus subtilis*. *Cell* **104**: 913-922.

Joyce, G., Williams, K.J., Robb, M., Noens, E., Tizzano, B., Shahrezaei, V., and Robertson, B.D. (2012) Cell division site placement and asymmetric growth in mycobacteria. *PloS One* **7**: e44582.

Jung, A., Eisheuer, S., Cserti, E., Leicht, O., Strobel, W., Möll, A., Schlimpert, S., Kühn, J., and Thanbichler, M. (2015) Molecular toolbox for genetic manipulation of the stalked budding bacterium *Hyphomonas neptunium*. *Appl Environ Microbiol* **81**: 736-744.

Korat, B., Mottl, H., and Keck, W. (1991) Penicillin-binding protein 4 of *Escherichia coli*: molecular cloning of the *dacB* gene, controlled overexpression, and alterations in murein composition. *Mol Microbiol* **5**: 675-684.

Kremer, J.R., Mastronarde, D.N., and McIntosh, J.R. (1996) Computer visualization of three-dimensional image data using IMOD. *J Struct Biol* **116**: 71-76.

Kuru, E., Hughes, H.V., Brown, P.J., Hall, E., Tekkam, S., Cava, F., de Pedro, M.A., Brun, Y.V., and VanNieuwenhze, M.S. (2012) *In situ* probing of newly synthesized peptidoglycan in live bacteria with fluorescent D-amino acids. *Angew Chem Int Ed Engl* **51**: 12519-12523.

Larkin, M.A., Blackshields, G., Brown, N.P., Chenna, R., McGettigan, P.A., McWilliam, H., Valentin, F., Wallace, I.M., Wilm, A., Lopez, R., Thompson, J.D., Gibson, T.J., and Higgins, D.G. (2007) Clustal W and Clustal X version 2.0. *Bioinformatics* **23**: 2947-2948.

Lee, T.K., Tropini, C., Hsin, J., Desmarais, S.M., Ursell, T.S., Gong, E., Gitai, Z., Monds, R.D., and Huang, K.C. (2014) A dynamically assembled cell wall synthesis machinery buffers cell growth. *Proc Natl Acad Sci U S A* **111**: 4554-4559.

Leifson, E. (1964) *Hyphomicrobium neptunium* sp. n. *Antonie Van Leeuwenhoek* **30**: 249-256.

Letek, M., Fiuza, M., Ordonez, E., Villadangos, A.F., Flardh, K., Mateos, L.M., and Gil, J.A. (2009) DivIVA uses an N-terminal conserved region and two coiled-coil domains to localize and sustain the polar growth in *Corynebacterium glutamicum*. *FEMS Microbiol Lett* **297**: 110-116.

Lutkenhaus, J., Pichoff, S., and Du, S. (2012) Bacterial cytokinesis: From Z ring to divisome. *Cytoskeleton* **69**: 778-790.

Magnet, S., Dubost, L., Marie, A., Arthur, M., and Gutmann, L. (2008) Identification of the L,D-transpeptidases for peptidoglycan cross-linking in *Escherichia coli*. *J Bacteriol* **190**: 4782-4785.

Mainardi, J.L., Fourgeaud, M., Hugonnet, J.E., Dubost, L., Brouard, J.P., Ouazzani, J., Rice, L.B., Gutmann, L., and Arthur, M. (2005) A novel peptidoglycan cross-linking enzyme for a beta-lactam-resistant transpeptidation pathway. *J Biol Chem* **280**: 38146-38152.

Margolin, W. (2009) Sculpting the bacterial cell. *Curr Biol* **19**: R812-822.

Mohammadi, T., van Dam, V., Sijbrandi, R., Vernet, T., Zapun, A., Bouhss, A., Diepeveen-de Bruin, M., Nguyen-Disteche, M., de Kruijff, B., and Breukink, E. (2011) Identification of FtsW as a transporter of lipid-linked cell wall precursors across the membrane. *EMBO J* **30**: 1425-1432.

Moore, R.L. (1981) The biology of *Hyphomicrobium* and other prosthecate, budding bacteria. *Annu Rev Microbiol* **35**: 567-594.

Morgenstein, R.M., Bratton, B.P., Nguyen, J.P., Ouzounov, N., Shaevitz, J.W., and Gitai, Z. (2015) RodZ links MreB to cell wall synthesis to mediate MreB rotation and robust morphogenesis. *Proc Natl Acad Sci U S A*.

Nguyen, L.T., Gumbart, J.C., Beeby, M., and Jensen, G.J. (2015) Coarse-grained simulations of bacterial cell wall growth reveal that local coordination alone can be sufficient to maintain rod shape. *Proc Natl Acad Sci U S A* **112**: E3689-3698.

Olshausen, P.V., Defeu Soufo, H.J., Wicker, K., Heintzmann, R., Graumann, P.L., and Rohrbach, A. (2013) Superresolution imaging of dynamic MreB filaments in *B. subtilis* – a multiple-motor-driven transport? *Biophys J* **105**: 1171-1181.

Pilhofer, M., Ladinsky, M.S., McDowall, A.W., and Jensen, G.J. (2010) Bacterial TEM: new insights from cryo-microscopy. *Methods Cell Biol* **96**: 21-45.

Poindexter, J.S. (1964) Biological properties and classification of the *Caulobacter* group. *Bacteriol Rev* **28**: 231-295.

R Development Core Team (2012) R: a language and environment for statistical computing. Vienna, Austria: The R Foundation for Statistical Computing.

Randich, A.M., and Brun, Y.V. (2015) Molecular mechanisms for the evolution of bacterial morphologies and growth modes. *Front Microbiol* **6**: 580.

Salje, J., van den Ent, F., de Boer, P., and Löwe, J. (2011) Direct membrane binding by bacterial actin MreB. *Mol Cell* **43**: 478-487.

Scheurwater, E., Reid, C.W., and Clarke, A.J. (2008) Lytic transglycosylases: bacterial space-making autolysins. *Int J Biochem Cell Biol* **40**: 586-591.

Schiffer, G., and Höltje, J.V. (1999) Cloning and characterization of PBP 1C, a third member of the multimodular class A penicillin-binding proteins of *Escherichia coli*. *J Biol Chem* **274**: 32031-32039.

Schindelin, J., Arganda-Carreras, I., Frise, E., Kaynig, V., Longair, M., Pietzsch, T., Preibisch, S., Rueden, C., Saalfeld, S., Schmid, B., Tinevez, J.Y., White, D.J., Hartenstein, V., Eliceiri, K., Tomancak, P., and Cardona, A. (2012) Fiji: an open-source platform for biological-image analysis. *Nat Methods* **9**: 676-682.

Schleifer, K.H., and Kandler, O. (1972) Peptidoglycan types of bacterial cell walls and their taxonomic implications. *Bacteriol Rev* **36**: 407-477.

Schlimpert, S., Klein, E.A., Briegel, A., Hughes, V., Kahnt, J., Bolte, K., Maier, U.G., Brun, Y.V., Jensen, G.J., Gitai, Z., and Thanbichler, M. (2012) General protein diffusion barriers create compartments within bacterial cells. *Cell* **151**: 1270-1282.

Schmidt, J.M., and Stanier, R.Y. (1966) The development of cellular stalks in bacteria. *J Cell Biol* **28**: 423-436.

Sham, L.T., Butler, E.K., Lebar, M.D., Kahne, D., Bernhardt, T.G., and Ruiz, N. (2014) Bacterial cell wall. MurJ is the flippase of lipid-linked precursors for peptidoglycan biogenesis. *Science* **345**: 220-222.

Shiomi, D., Sakai, M., and Niki, H. (2008) Determination of bacterial rod shape by a novel cytoskeletal membrane protein. *EMBO J* **27**: 3081-3091.

Spratt, B.G. (1975) Distinct penicillin binding proteins involved in the division, elongation, and shape of *Escherichia coli* K12. *Proc Natl Acad Sci U S A* **72**: 2999-3003.

Strobel, W., Möll, A., Kiekebusch, D., Klein, K.E., and Thanbichler, M. (2014) Function and localization dynamics of bifunctional penicillin-binding proteins in *Caulobacter crescentus*. *J Bacteriol* **196**: 1627-1639.

Suginaka, H., Blumberg, P.M., and Strominger, J.L. (1972) Multiple penicillin-binding components in *Bacillus subtilis*, *Bacillus cereus*, *Staphylococcus aureus*, and *Escherichia coli*. *J Biol Chem* **247**: 5279-5288.

Swulius, M.T., and Jensen, G.J. (2012) The helical MreB cytoskeleton in E*scherichia coli* MC1000/pLE7 is an artifact of the N-terminal yellow fluorescent protein tag. *J Bacteriol* **194**: 6382-6386.

Takacs, C.N., Hocking, J., Cabeen, M.T., Bui, N.K., Poggio, S., Vollmer, W., and Jacobs-Wagner, C. (2013) Growth medium-dependent glycine incorporation into the peptidoglycan of *Caulobacter crescentus*. *PloS One* **8**: e57579.

Takacs, C.N., Poggio, S., Charbon, G., Pucheault, M., Vollmer, W., and Jacobs-Wagner, C. (2010) MreB drives de novo rod morphogenesis in *Caulobacter crescentus* via remodeling of the cell wall. *J Bacteriol* **192**: 1671-1684.

Thanbichler, M., and Shapiro, L. (2006) MipZ, a spatial regulator coordinating chromosome segregation with cell division in *Caulobacter*. *Cell* **126**: 147-162.

Tivol, W.F., Briegel, A., and Jensen, G.J. (2008) An improved cryogen for plunge freezing. *Microsc Microanal* **14:** 375-379.

Typas, A., Banzhaf, M., Gross, C.A., and Vollmer, W. (2012) From the regulation of peptidoglycan synthesis to bacterial growth and morphology. *Nat Rev Microbiol* **10**: 123-136.

Uehara, T., and Bernhardt, T.G. (2011) More than just lysins: peptidoglycan hydrolases tailor the cell wall. *Curr Opin Microbiol* **14**: 698-703.

Uehara, T., Parzych, K.R., Dinh, T., and Bernhardt, T.G. (2010) Daughter cell separation is controlled by cytokinetic ring-activated cell wall hydrolysis. *EMBO J* **29**: 1412-1422.

van den Ent, F., Amos, L.A., and Löwe, J. (2001) Prokaryotic origin of the actin cytoskeleton. *Nature* **413**: 39-44.

van den Ent, F., Izore, T., Bharat, T.A., Johnson, C.M., and Löwe, J. (2014) Bacterial actin MreB forms antiparallel double filaments. *Elife* **3**: e02634.

van Heijenoort, J. (2001) Formation of the glycan chains in the synthesis of bacterial peptidoglycan. *Glycobiology* **11**: 25R-36R.

Van Heijenoort, Y., and Van Heijenoort, J. (1971) Study of the N-acetylmuramyl-L-alanine amidase activity in *Escherichia coli*. *FEBS Lett* **15**: 137-141.

van Teeffelen, S., Wang, S., Furchtgott, L., Huang, K.C., Wingreen, N.S., Shaevitz, J.W., and Gitai, Z. (2011) The bacterial actin MreB rotates, and rotation depends on cell-wall assembly. *Proc Natl Acad Sci U S A* **108**: 15822-15827.

Vollmer, W., and Bertsche, U. (2008) Murein (peptidoglycan) structure, architecture and biosynthesis in *Escherichia coli*. *Biochim Biophys Acta* **1778**: 1714-1734.

Vollmer, W., Blanot, D., and de Pedro, M.A. (2008) Peptidoglycan structure and architecture. *FEMS Microbiol Rev* **32**: 149-167.

Wagner, J.K., Galvani, C.D., and Brun, Y.V. (2005) *Caulobacter crescentus* requires RodA and MreB for stalk synthesis and prevention of ectopic pole formation. *J Bacteriol* **187**: 544-553.

Wali, T.M., Hudson, G.R., Danald, D.A., and Weiner, R.M. (1980) Timing of swarmer cell cycle morphogenesis and macromolecular synthesis by *Hyphomicrobium neptunium* in synchronous culture. *J Bacteriol* **144**: 406-412.

Weiss, D.S., Chen, J.C., Ghigo, J.M., Boyd, D., and Beckwith, J. (1999) Localization of FtsI (PBP3) to the septal ring requires its membrane anchor, the Z ring, FtsA, FtsQ, and FtsL. *J Bacteriol* **181**: 508-520.

Whittenbury, R., and Dow, C.S. (1977) Morphogenesis and differentiation in *Rhodomicrobium vannielii* and other budding and prosthecate bacteria. *Bacteriol Rev* **41**: 754-808.

Whittenbury, R., and McLee, A.G. (1967) *Rhodopseudomonas palustris* and *Rh. viridis* – photosynthetic budding bacteria. *Arch Mikrobiol* **59**: 324-334.

Williams, M., Hoffman, M.D., Daniel, J.J., Madren, S.M., Dhroso, A., Korkin, D., Givan, S.A., Jacobson, S.C., and Brown, P.J. (2016) Short-stalked *Prosthecomicrobium hirschii* cells have a *Caulobacter*-like cell cycle. *J Bacteriol* **198**: 1149-1159.

Yang, J., Yan, R., Roy, A., Xu, D., Poisson, J., and Zhang, Y. (2015) The I-TASSER Suite: protein structure and function prediction. *Nature methods* **12**: 7-8.

Young, K.D. (2006) The selective value of bacterial shape. *Microbiol Mol Biol Rev* **70**: 660-703.

Zerfas, P.M., Kessel, M., Quintero, E.J., and Weiner, R.M. (1997) Fine-structure evidence for cell membrane partitioning of the nucleoid and cytoplasm during bud formation in *Hyphomonas* species. *J Bacteriol* **179**: 148-156.

Zheng, S.Q., Keszthelyi, B., Branlund, E., Lyle, J.M., Braunfeld, M.B., Sedat, J.W., and Agard, D.A. (2007) UCSF tomography: an integrated software suite for real-time electron microscopic tomographic data collection, alignment, and reconstruction. *J Struct Biol* **157**: 138-147.

FIGURE LEGENDS

Figure 1. Phylogeny of alphaproteobacteria with asymmetric growth patterns. Shown is the phylogeny of representative alphaproteobacteria known to exhibit polar growth, budding, and/or stalk formation, based on a comparison of GyrA protein sequences. The classification of the different species and typical examples of morphologies observed in the indicated families are given next to the tree. Statistical support for branches is indicated by bootstrap values (100 trials). The scale bar represents the number of substitutions per site. The node at which MreB and the associated proteins MreCD, RodA, RodZ, and PBP2 are predicted to have been lost (Brown *et al.*, 2012) is labeled with a red dot.

Figure 2. Ultrastructure of *H. neptunium* at different stages of the cell cycle. *H. neptunium* wild-type cells were grown to exponential phase in MB medium and analyzed by electron cryo-tomography. Shown are virtual sections through reconstructions of **(A)** a swarmer cell, **(B,C)** early stalked cells, **(D)** the terminal region of the stalk before the onset of bud formation, **(E,F,G)** the bud compartment at different stages of the budding process, and **(H)** a mature bud immediately before its release from the mother cell. Arrowheads point to polar flagella. The asterisk indicates the cell division site. IM, inner membrane. OM, outer membrane. P, peptidoglycan. N, nucleoid. Scale bars: 100 nm.

Figure 3. Growth dynamics of *H. neptunium*. (A) Time-lapse analysis showing the developmental cycle of a single *H. neptunium* cell during exponential growth in a microfluidic flow cell. Shown are DIC images taken at the indicated time points after the start of the experiment. Scale bar: 2 µm. **(B)** Quantification of the lengths of the mother cell body (light grey), the stalk (dark grey), and the bud compartment (red) over the course of many division cycles. A single cell growing in a microfluidic flow cell was imaged by DIC microscopy at 15 min intervals. Arrows indicate the first frame taken after a cell division event. The data are based on Movie S1. **(C)** Fluorescent labeling of the zones of active PG incorporation. Exponentially growing wild-type cells were pulse-labeled with the fluorescent D-amino acid derivative HADA and imaged by DIC and fluorescence microscopy. Shown are representative images of cells at different stages of the cell cycle. Scale bar: 2 µm. **(D)** Demograph analysis showing the distribution of HADA fluorescence in a random subpopulation of cells treated as described in (C). To generate the graph, fluorescence profiles were normalized and stacked on top of each other according to cell length.

Figure 4. **Muropeptide profile of *H. neptunium* cell walls. (A)** UPLC profiles of muropeptides from *H. neptunium* (blue) and *C. crescentus* (red). PG sacculi isolated from exponentially growing cells were digested with mutanolysin, and the resulting muropeptides were separated by reversed-phase chromatography. The elution position of muropeptides with a tripeptide side chain is indicated by an

asterisk. **(B)** Graphical representation of the major muropeptide species. Shown are the structures of the most abundant muropeptides and their relative abundance in the traces shown in (A).

Figure 5. Role and localization patterns of peptidoglycan hydrolases in *H. neptunium*. (A) Schematic overview of all putative PG hydrolases encoded in the *H. neptunium* genome. Shown are the different hydrolase families and the domain structures of their members. The corresponding ORF numbers are given in **Table S1**. CC, coiled-coil region. TM, transmembrane domain. SP, signal peptide. The potentially essential hydrolase LmdC is indicated in red. Asterisks mark mutations in catalytically important residues. **(B)** Phenotypes of PG hydrolase mutants. The *H. neptunium* wild type (WT) and strains EC39 (*ΔlmdE*), SR11 (*ΔdacB*), EC95 (*ΔmltA*), SR07 (*ΔgplA*), and SR18 (*ΔamiC*) were grown to exponential phase and visualized by DIC microscopy. Scale bars: 3 µm. **(C)** Cell lengths of PG hydrolase mutants. Cells from (A) were analyzed for their cell lengths. The data are shown as box plots, with the bar indicating the median, the box the interquartile range, and the whiskers the 5th and 95th percentile. Distributions significantly different from that of the WT are indicated (***; t-test, $p < 10^{-5}$). n = 200 per strain. **(D)** Localization pattern of DacL. Strain SR28 (*dacL-mCherry*) was grown to exponential phase and imaged by DIC and fluorescence microscopy. Shown are representative cells at different stages of the cell cycle. Scale bar: 2 µm. **(E)** Localization pattern of AmiC. Cells of strain EC70 (P_{cu}::P_{cu}-*amiC-mCherry*) were grown to exponential phase, induced for 24 h with 300 µM $CuSO_4$, and imaged by DIC and fluorescence microscopy. Scale bar: 2 µm. **(F)** Demographs showing the distribution of DacL-mCherry and AmiC-mCherry in cells analyzed as described in (D) and (E). Note that, due to by the variability of the stalk and bud lengths, the profiles of late pre-divisional cells showing an AmiC-mCherry focus are scattered throughout the bottom half of the graph.

Figure 6. Role and localization patterns of peptidoglycan synthases in *H. neptunium*. (A) Schematic overview of all putative PG synthases encoded in the *H. neptunium* genome. Shown are the different enzyme families and the domain structures of their members. The corresponding ORF numbers are listed in **Table S1**. TM, transmembrane domain. SP, signal peptide. TG, transglycosylase. TP, trans-peptidase. Potentially essential proteins are indicated in red. **(B)** Phenotypes of PG synthase mutants. The *H. neptunium* wild type (WT) and strains EC26 (*Δpbp1X*), EC27 (*Δpbp1C*), and EC57 (*Δpbp1X Δpbp1C*) were grown to exponential phase and analyzed by DIC microscopy. Scale bar: 3 µm. **(C)** Cells lengths of PG synthase mutants. Cells from the analysis described in (B) were subjected to cell lengths measurements. The data are shown as box plots, as explained in Figure 5C. Distributions significantly different from that of the WT are indicated (***; t-test, $p < 10^{-15}$). n = 200 per strain. **(D,E)** Localization

patterns of Venus-PBP2 and Venus-PBP3. Cells of strains SR14 (*venus-pbp2*) and SE161 (*venus-pbp3*) were grown to exponential phase and imaged by DIC and fluorescence microscopy. Shown are representative images of cells at different stages of the cell cycle. Scale bar: 2 µm. **(F)** Demographs showing the localization patterns of Venus-PBP2 in a mixed population of cells and Venus-PBP3 in budding cells, analyzed as described in (D,E). Note that, due to by the variability of the stalk and bud lengths, the profiles of late pre-divisional budding cells showing a Venus-PBP3 focus are scattered throughout the graph.

Figure 7. Localization patterns of the elongasome components MreB and RodZ. (A) Structural model of *H. neptunium* MreB. The inset shows the site used to insert the mCherry tag. **(B,D)** Localization patterns of MreB-mCherry^{SW} and YFP-RodZ. Cells of strains EC63 (*mreB-mCherry^{SW}*) and EC93 (*yfp-rodZ*) were grown to exponential phase and analyzed by DIC and fluorescence microscopy. Shown are representative images of cells at different stages of the cell cycle. Scale bar: 2 µm. **(C,E)** Demographs showing the localization patterns of MreB-mCherry^{SW} and YFP-RodZ in random subpopulations of cells, analyzed as described in (B,D).

Figure 8. Aberrant cell shape after inhibition of MreB with the small molecule MP265. (A) Inhibition of growth by the MreB inhibitor MP265. Exponentially growing cells of the *H. neptunium* wild-type strain were diluted into fresh media containing different concentrations of MP265. Subsequently, their growth was monitored for 30 h using a microplate reader. **(B)** Effect of MP265 on cell morphology. Cells were grown to exponential phase and exposed for 24 h to 250 µM MP265. After washing and resuspension in medium lacking the inhibitor, cells were cultivated further to monitor the gradual recovery of wild-type morphology. Samples were taken at the indicated time points after addition (+) or removal (-) of MP265 and analyzed by DIC microscopy. Aberrant stalks are indicated by arrowheads. Scale bar: 3 µm. **(C,D)** Quantitative analysis of changes in cell shape after MP265 treatment. Cells were grown to exponential phase and exposed to the indicated concentrations of MP265 for 24 h. After imaging by DIC microscopy, the lengths (C) and widths (D) of their cell bodies (excluding stalks and buds) were measured. The data are shown as box plots, as described in Figure 5C. Distributions significantly different from that of the control culture (0 µM) are indicated (***; t-test, $p < 10^{-5}$ in C and $p < 10^{-17}$ in D). n = 100 for each concentration.

Figure 9. Main growth zones of *H. neptunium*, *A. tumefaciens*, and *C. crescentus*. *H. neptunium* exhibits four distinct growth zones (red), alternating between disperse and zonal PG incorporation. *A. tumefaciens* elongates by polar growth and then divides by zonal growth at the cell center (Brown *et al.*,

2012; Cameron *et al.*, 2014). *C. crescentus* elongates by dispersed and preseptal zonal growth and divides by zonal growth at midcell. Its stalk emerges by zonal growth at the stalk base (Aaron *et al.*, 2007). See text for details.

TABLE

Table 1. Muropeptide profile of *H. neptunium*.

Muropeptide	*H. neptunium* (%) [1]			*C. crescentus* (%) [1]		
	Average		SD	Average		SD
Tri/Tri without GlcNAc	0	±	0	0.91	±	0.76
Tetra-Tetra-Tetra-Tetra	0.73	±	0.07	0	±	0
Tetra-Tetra-Tetra-anhydro	1.32	±	1.05	2.07	±	0.65
Tetra-Tetra-Tetra	0	±	0	1.29	±	0.07
Tetra-Tetra-Penta-anhydro	0	±	0	1.16	±	0.22
Tetra-Tetra-anhydro	7.77	±	0.33	1.71	±	0.57
Tetra-Tetra	12.04	±	3.76	5.22	±	1.64
Tetra-Tetra dianhydro	2.26	±	2.49	0	±	0
Tetra-Penta-anhydro	0	±	0	1.10	±	0.05
Tetra-Penta (Gly^5)-anhydro	0.37	±	0.15	1.32	±	0.86
Tetra-Penta (Gly^5)	6.79	±	4.77	4.09	±	0.90
Tetra-Penta	0	±	0	4.04	±	1.32
Tetra-anhydro	0.10	±	0.09	3.55	±	1.42
Tetra (Gly^4)	0	±	0	0.73	±	0.67
Tetra	36.87	±	2.48	21.07	±	2.65
Penta	0	±	0	10.62	±	1.34
Penta-anhydro	0	±	0	2.67	±	1.94
Penta (Gly^5)-Tetra-Tetra-anhydro	0	±	0	1.39	±	0.56
Penta (Gly^5)	3.21	±	0.79	9.81	±	1.58
Other	28.58	±	0.05	27.23	±	7.85
All known	71.43	±	0.07	72.78	±	7.86
Monomers (total)	56.24	±	3.86	67.98	±	2.48
Dimers (total)	40.90	±	2.30	23.79	±	4.64
Trimers (total)	1.84	±	1.47	8.23	±	2.16
Tetramers (total)	1.02	±	0.09	0	±	0
Tripeptides (total)	0	±	0	1.32	±	1.19
Tetrapeptides (total)	90.50	±	3.66	58.44	±	2.36
Pentapeptides (total)	9.50	±	3.66	40.24	±	1.17
Chain ends (anhydro-disaccharide units)	9.61	±	3.97	13.61	±	1.69
Average chain length	11.38	±	4.70	7.41	±	0.92
Degree of cross-linkage	22.44	±	2.20	17.38	±	0.88
% Peptides in cross-links	43.76	±	3.86	32.02	±	2.48

[1] **Shown are the average values obtained from two experiments.**

The stalked budding bacterium *Hyphomonas neptunium* grows by generating buds at the tip of a stalk-like cellular extension. This study reports the first molecular-level analysis of cell wall biosynthesis in this species. We show that its mode of growth differs significantly from that in related polarly growing species and identify factors critical to proper morphogenesis. These findings set the stage for in-depth mechanistic studies of a fascinating but poorly understood mode of bacterial proliferation.

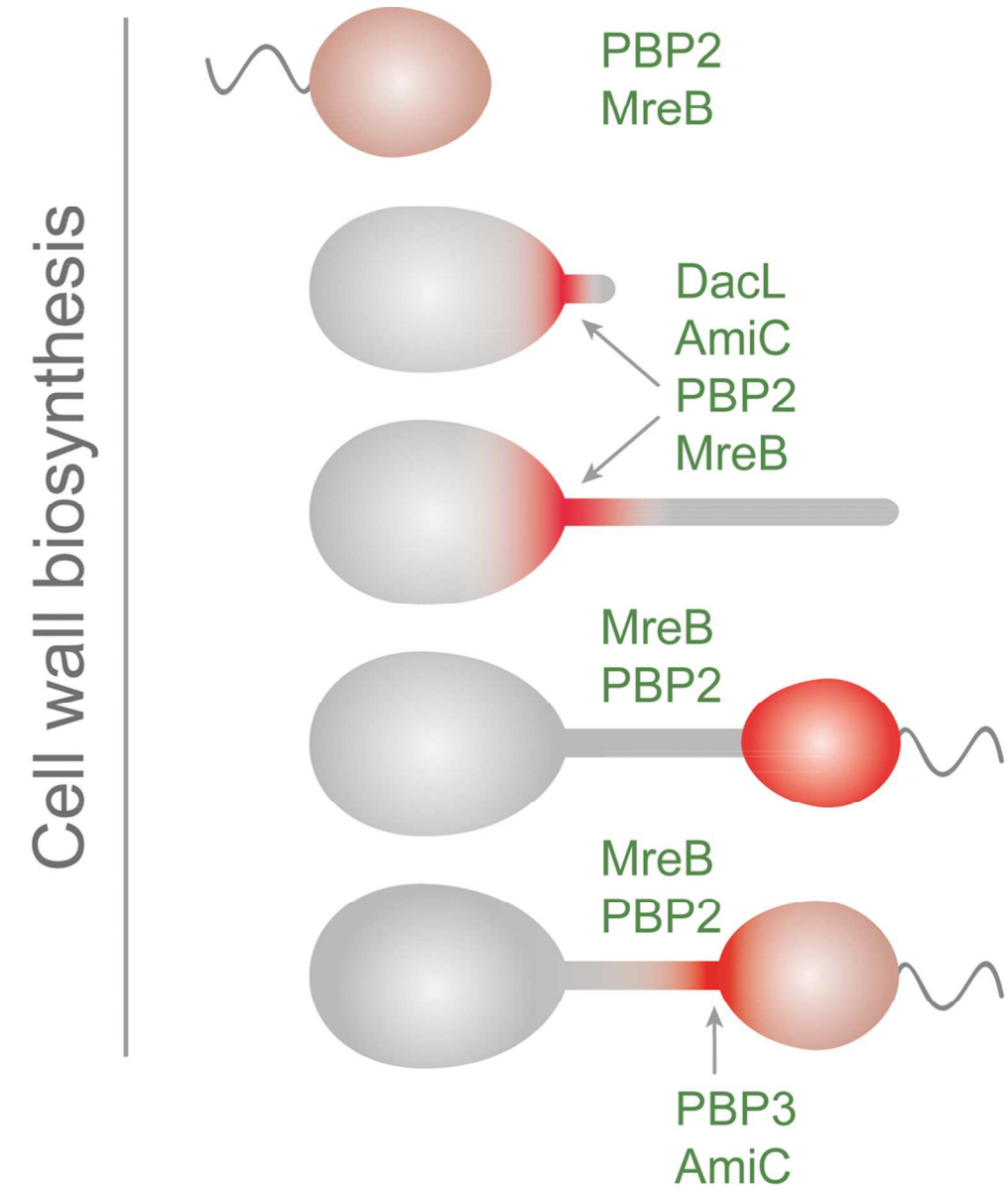

88x107mm (300 x 300 DPI)

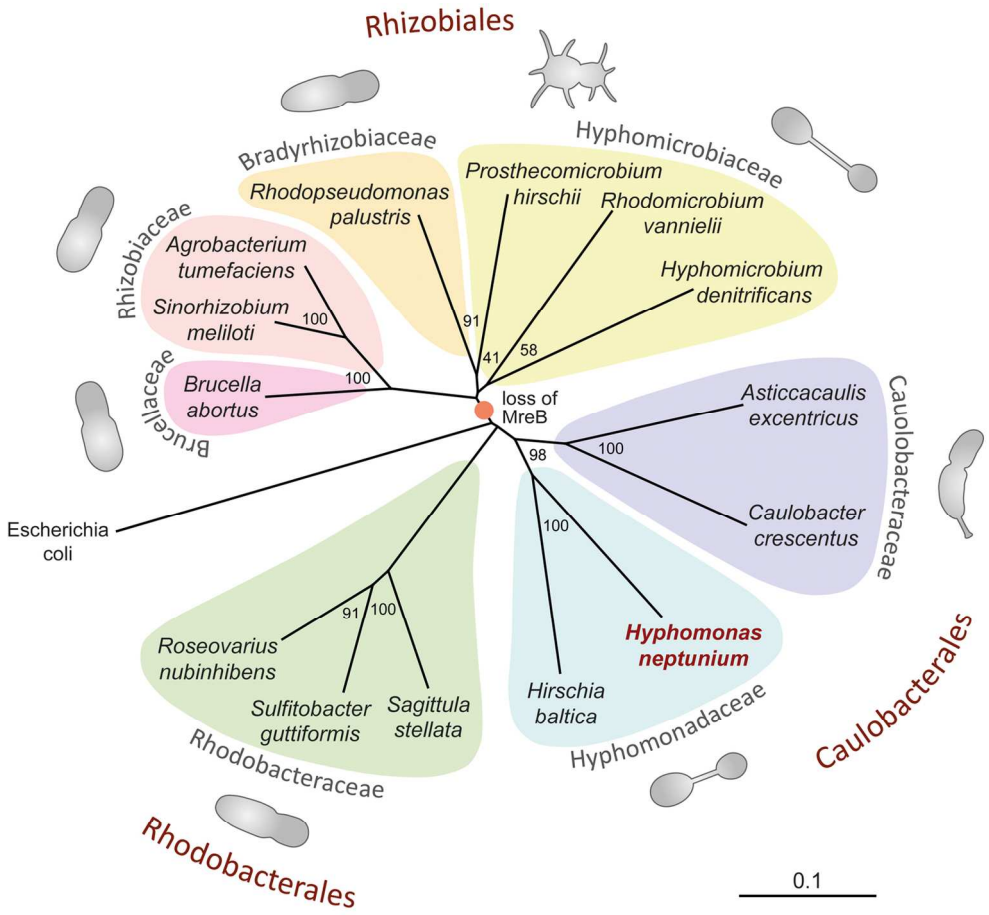

Figure 1. Phylogeny of alphaproteobacteria with asymmetric growth patterns. Shown is the phylogeny of representative alphaproteobacteria known to exhibit polar growth, budding, and/or stalk formation, based on a comparison of GyrA protein sequences. The classification of the different species and typical examples of morphologies observed in the indicated families are given next to the tree. Statistical support for branches is indicated by bootstrap values (100 trials). The scale bar represents the number of substitutions per site. The node at which MreB and the associated proteins MreCD, RodA, RodZ, and PBP2 are predicted to have been lost (Brown et al., 2012) is labeled with a red dot.

135x124mm (300 x 300 DPI)

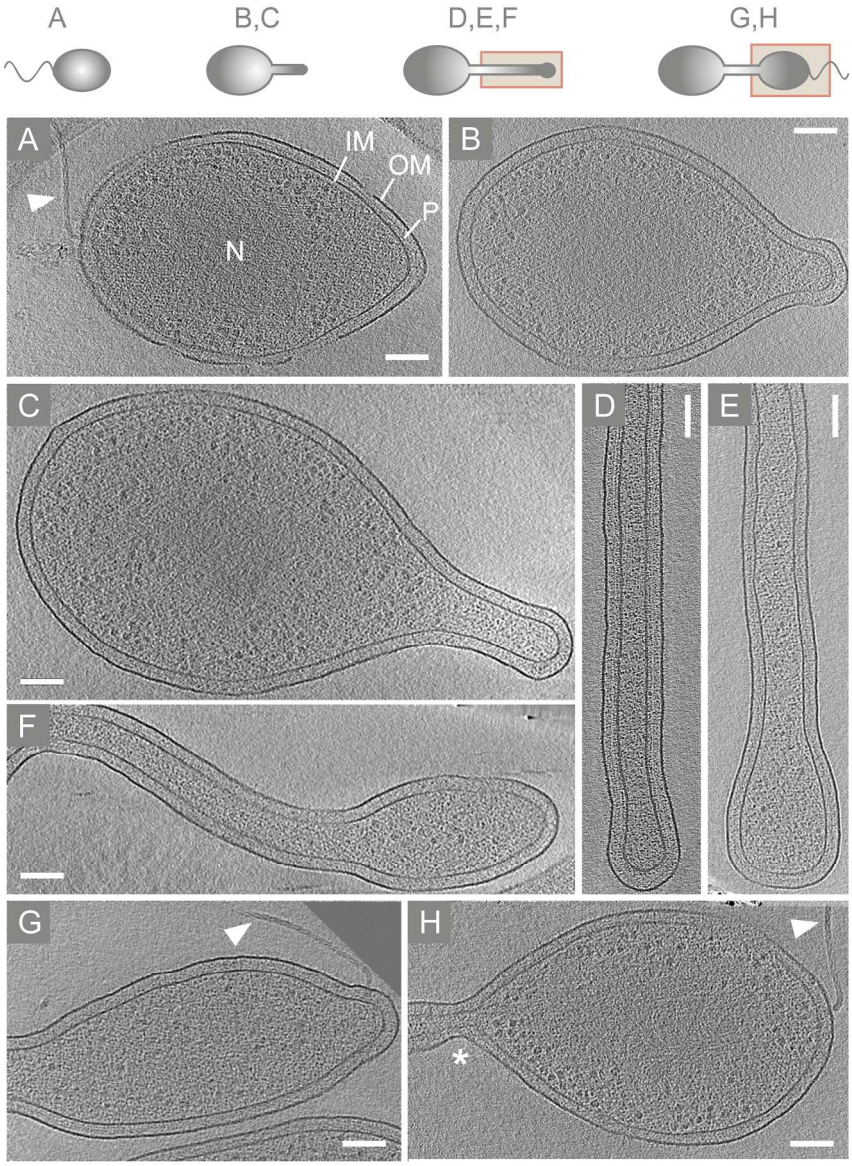

Figure 2. Ultrastructure of H. neptunium at different stages of the cell cycle. H. neptunium wild-type cells were grown to exponential phase in MB medium and analyzed by electron cryo-tomography. Shown are virtual sections through reconstructions of (A) a swarmer cell, (B,C) early stalked cells, (D) the terminal region of the stalk before the onset of bud formation, (E,F,G) the bud compartment at different stages of the budding process, and (H) a mature bud immediately before its release from the mother cell. Arrowheads point to polar flagella. The asterisk indicates the cell division site. IM, inner membrane. OM, outer membrane. P, peptidoglycan. N, nucleoid. Scale bars: 100 nm.

187x251mm (300 x 300 DPI)

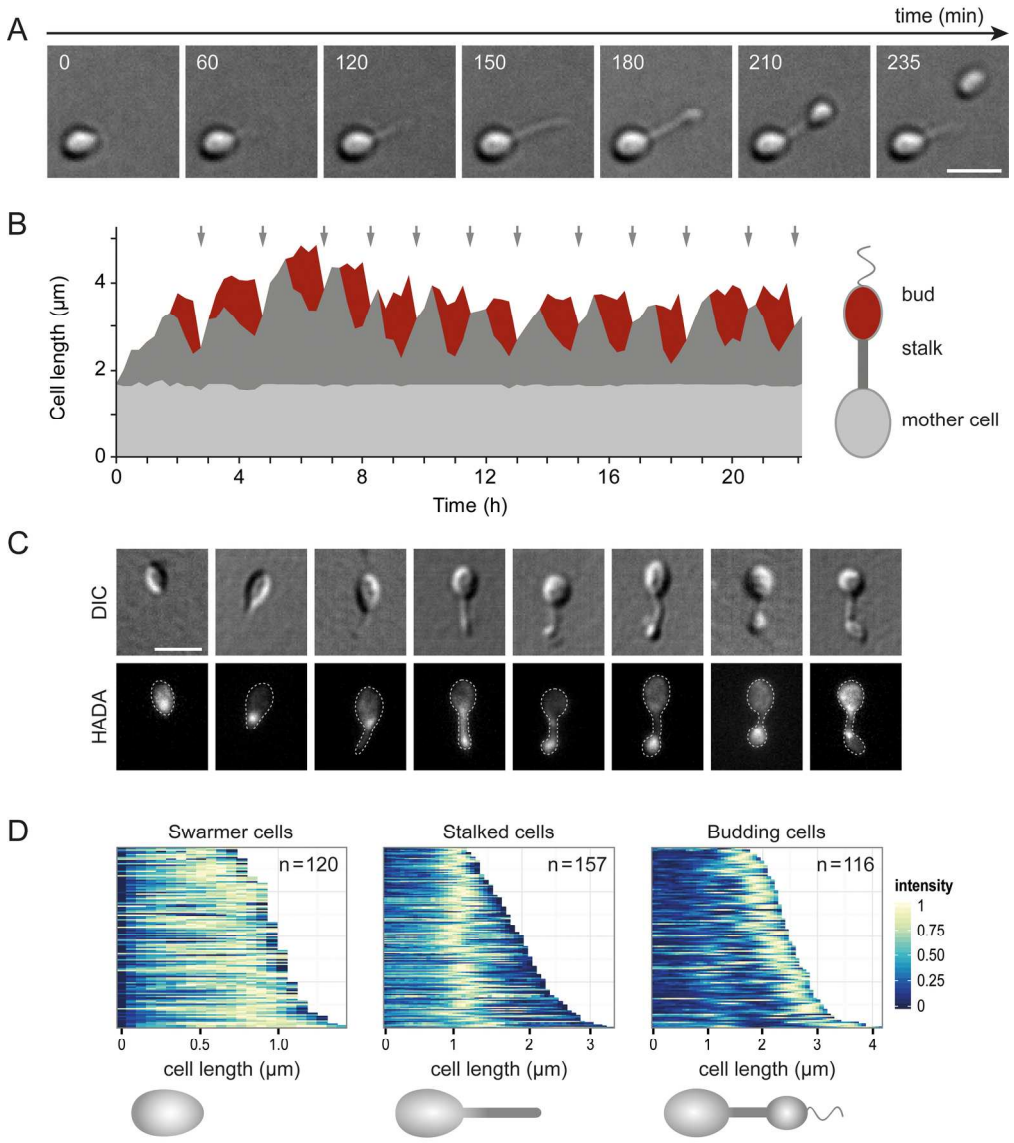

Figure 3. Growth dynamics of H. neptunium. (A) Time-lapse analysis showing the developmental cycle of a single H. neptunium cell during exponential growth in a microfluidic flow cell. Shown are DIC images taken at the indicated time points after the start of the experiment. Scale bar: 2 µm. (B) Quantification of the lengths of the mother cell body (light grey), the stalk (dark grey), and the bud compartment (red) over the course of many division cycles. A single cell growing in a microfluidic flow cell was imaged by DIC microscopy at 15 min intervals. Arrows indicate the first frame taken after a cell division event. The data are based on Movie S1. (C) Fluorescent labeling of the zones of active PG incorporation. Exponentially growing wild-type cells were pulse-labeled with the fluorescent D-amino acid derivative HADA and imaged by DIC and fluorescence microscopy. Shown are representative images of cells at different stages of the cell cycle. Scale bar: 2 µm. (D) Demograph analysis showing the distribution of HADA fluorescence in a random subpopulation of cells treated as described in (C). To generate the graph, fluorescence profiles were normalized and stacked on top of each other according to cell length.

180x205mm (300 x 300 DPI)

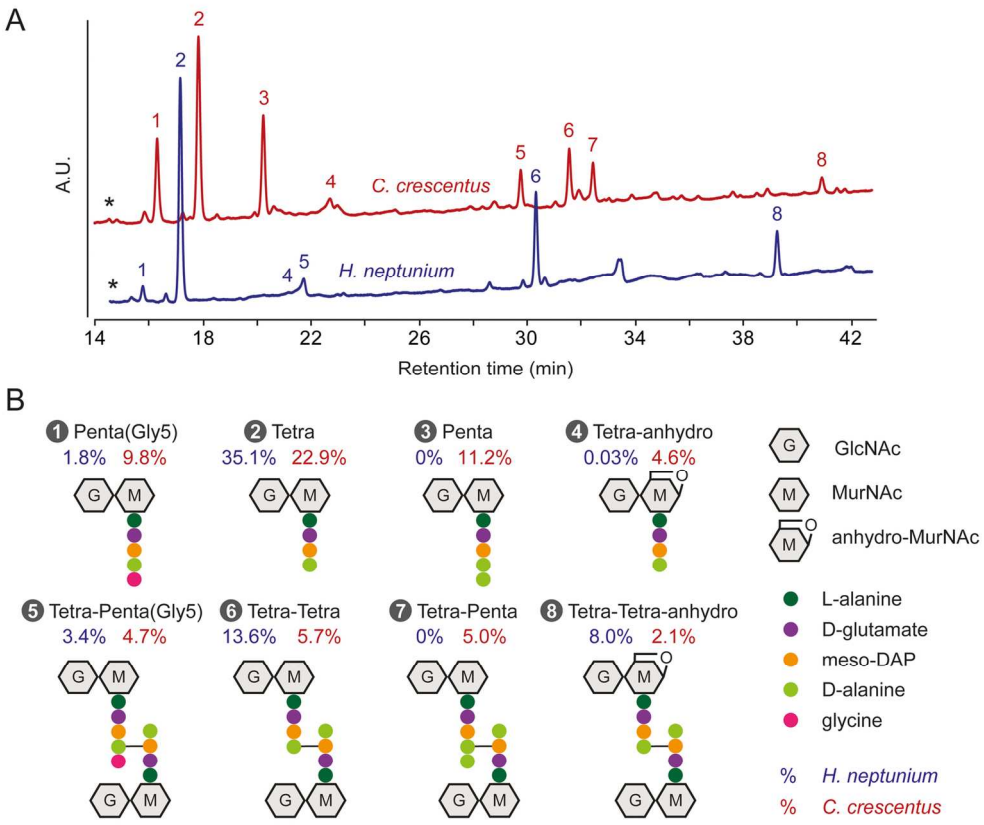

Figure 4. Muropeptide profile of H. neptunium cell walls. (A) UPLC profiles of muropeptides from H. neptunium (blue) and C. crescentus (red). PG sacculi isolated from exponentially growing cells were digested with mutanolysin, and the resulting muropeptides were separated by reversed-phase chromatography. The elution position of muropeptides with a tripeptide side chain is indicated by an asterisk. (B) Graphical representation of the major muropeptide species. Shown are the structures of the most abundant muropeptides and their relative abundance in the traces shown in (A).

142x124mm (300 x 300 DPI)

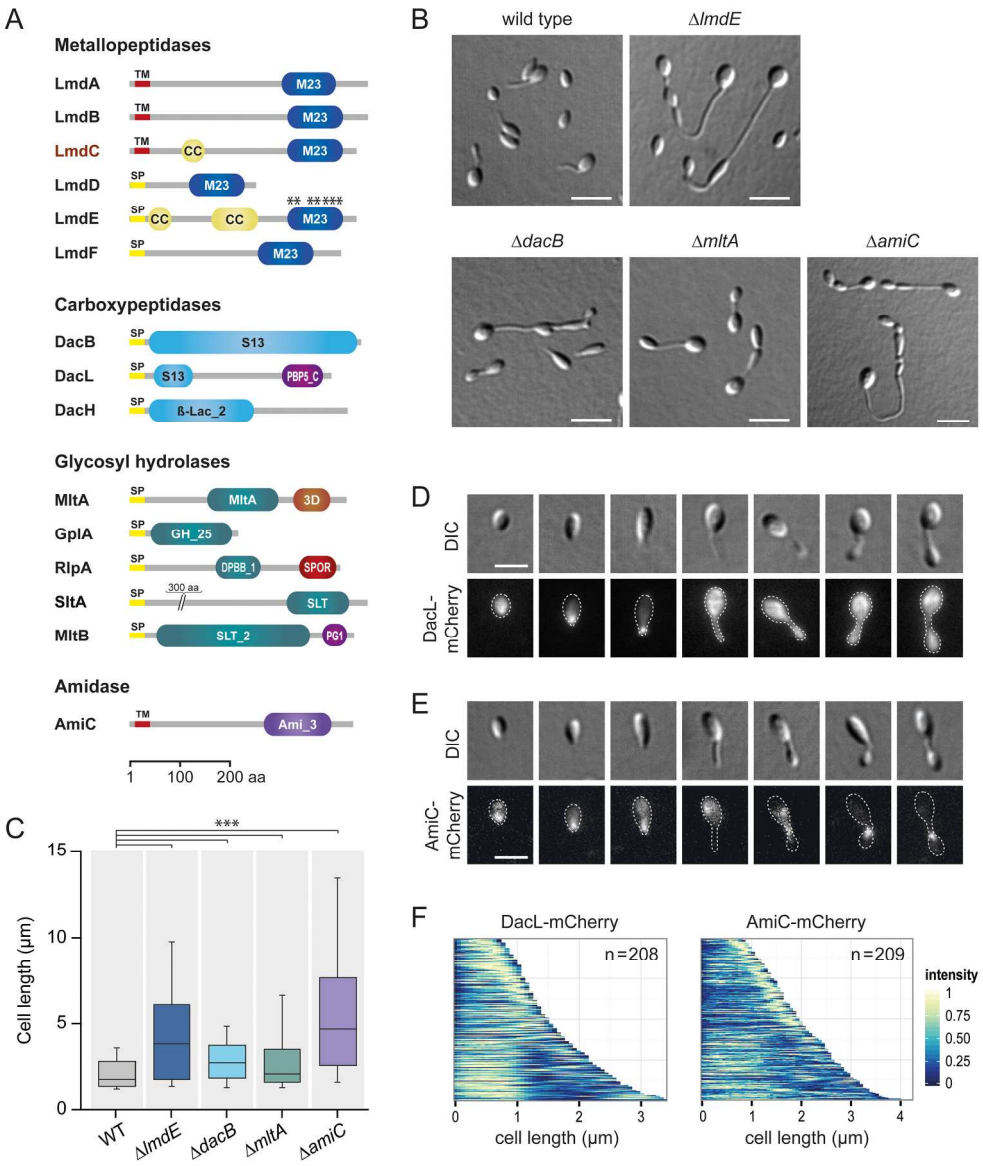

Figure 5. Role and localization patterns of peptidoglycan hydrolases in H. neptunium. (A) Schematic overview of all putative PG hydrolases encoded in the H. neptunium genome. Shown are the different hydrolase families and the domain structures of their members. The corresponding ORF numbers are given in Table S1. CC, coiled-coil region. TM, transmembrane domain. SP, signal peptide. The potentially essential hydrolase LmdC is indicated in red. Asterisks mark mutations in catalytically important residues. (B) Phenotypes of PG hydrolase mutants. The H. neptunium wild type (WT) and strains EC39 (ΔlmdE), SR11 (ΔdacB), EC95 (ΔmltA), SR07 (ΔgplA), and SR18 (ΔamiC) were grown to exponential phase and visualized by DIC microscopy. Scale bars: 3 µm. (C) Cell lengths of PG hydrolase mutants. Cells from (A) were analyzed for their cell lengths. The data are shown as box plots, with the bar indicating the median, the box the interquartile range, and the whiskers the 5th and 95th percentile. Distributions significantly different from that of the WT are indicated (***; t-test, $p < 10\text{-}5$). n = 200 per strain. (D) Localization pattern of DacL. Strain SR28 (dacL-mCherry) was grown to exponential phase and imaged by DIC and fluorescence microscopy. Shown are representative cells at different stages of the cell cycle. Scale bar: 2 µm. (E) Localization pattern of AmiC. Cells of strain EC70 (Pcu::Pcu-amiC-mCherry) were grown to exponential

phase, induced for 24 h with 300 µM CuSO4, and imaged by DIC and fluorescence microscopy. Scale bar: 2 µm. (F) Demographs showing the distribution of DacL-mCherry and AmiC-mCherry in cells analyzed as described in (D) and (E). Note that, due to by the variability of the stalk and bud lengths, the profiles of late pre-divisional cells showing an AmiC-mCherry focus are scattered throughout the bottom half of the graph.

207x244mm (300 x 300 DPI)

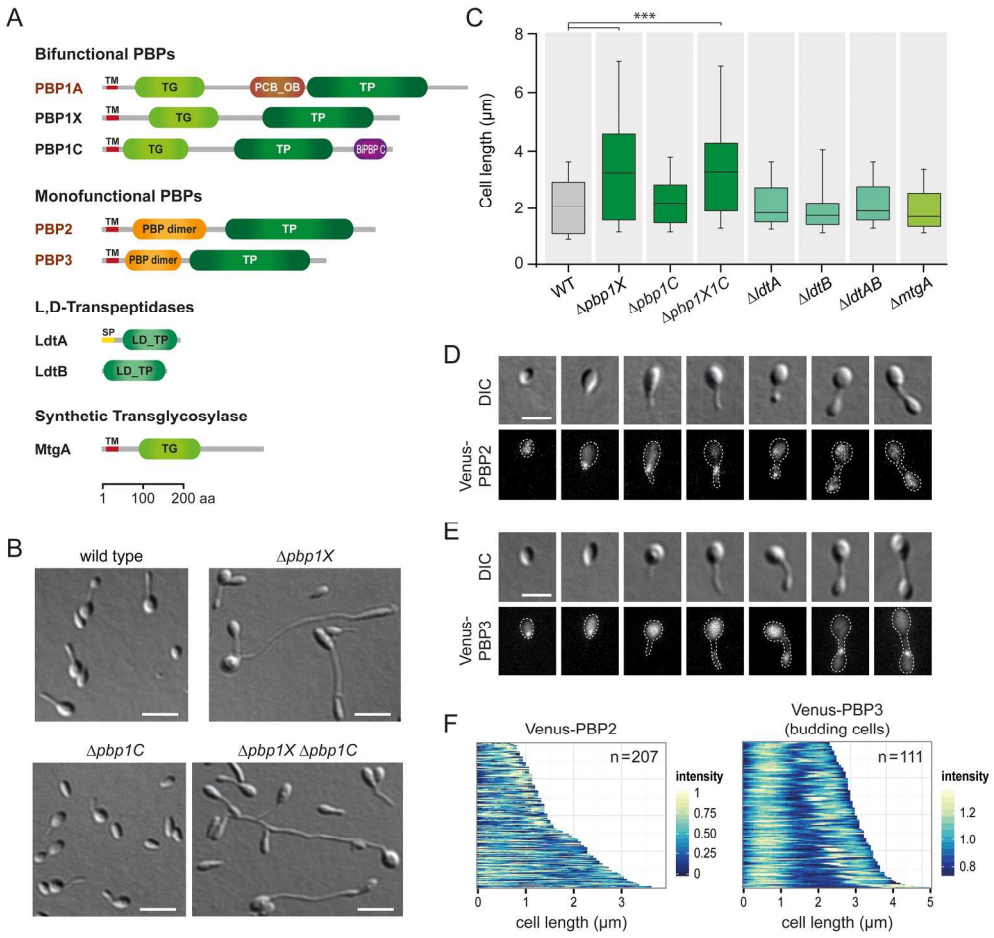

Figure 6. Role and localization patterns of peptidoglycan synthases in H. neptunium. (A) Schematic overview of all putative PG synthases encoded in the H. neptunium genome. Shown are the different enzyme families and the domain structures of their members. The corresponding ORF numbers are listed in Table S1. TM, transmembrane domain. SP, signal peptide. TG, transglycosylase. TP, trans¬peptidase. Potentially essential proteins are indicated in red. (B) Phenotypes of PG synthase mutants. The H. neptunium wild type (WT) and strains EC26 (Δpbp1X), EC27 (Δpbp1C), and EC57 (Δpbp1X Δpbp1C) were grown to exponential phase and analyzed by DIC microscopy. Scale bar: 3 μm. (C) Cells lengths of PG synthase mutants. Cells from the analysis described in (B) were subjected to cell lengths measurements. The data are shown as box plots, as explained in Figure 5C. Distributions significantly different from that of the WT are indicated (***; t-test, $p < 10\text{-}15$). n = 200 per strain. (D,E) Localization patterns of Venus-PBP2 and Venus-PBP3. Cells of strains SR14 (venus-pbp2) and SE161 (venus-pbp3) were grown to exponential phase and imaged by DIC and fluorescence microscopy. Shown are representative images of cells at different stages of the cell cycle. Scale bar: 2 μm. (F) Demographs showing the localization patterns of Venus-PBP2 in a mixed population of cells and Venus-PBP3 in budding cells, analyzed as described in (D,E). Note that, due to by the variability of the stalk and bud lengths, the profiles of late pre-divisional budding cells showing a Venus-PBP3 focus are scattered throughout the graph.

185x175mm (300 x 300 DPI)

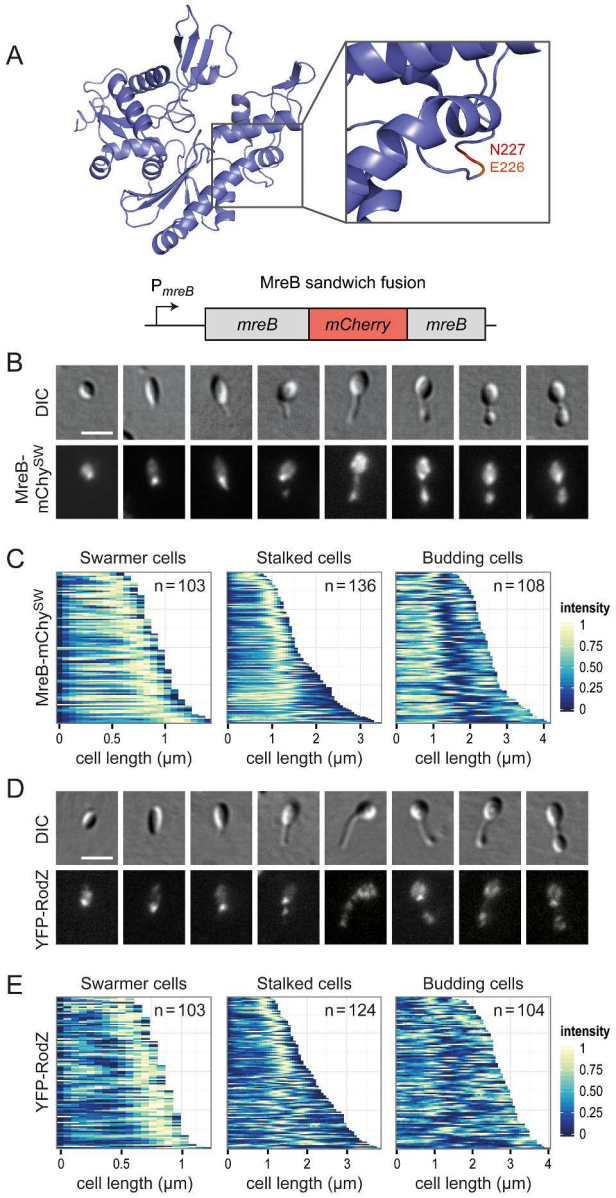

Figure 7. Localization patterns of the elongasome components MreB and RodZ. (A) Structural model of H. neptunium MreB. The inset shows the site used to insert the mCherry tag. (B,D) Localization patterns of MreB-mCherrySW and YFP-RodZ. Cells of strains EC63 (mreB-mCherrySW) and EC93 (yfp-rodZ) were grown to exponential phase and analyzed by DIC and fluorescence microscopy. Shown are representative images of cells at different stages of the cell cycle. Scale bar: 2 μm. (C,E) Demographs showing the localization patterns of MreB-mCherrySW and YFP-RodZ in random subpopulations of cells, analyzed as described in (B,D).

224x439mm (300 x 300 DPI)

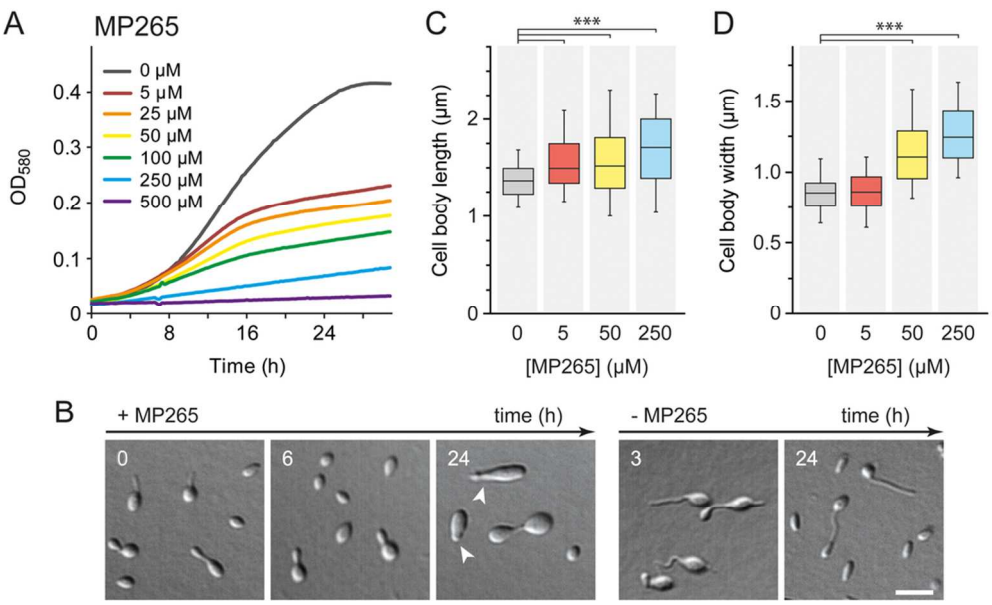

Figure 8. Aberrant cell shape after inhibition of MreB with the small molecule MP265. (A) Inhibition of growth by the MreB inhibitor MP265. Exponentially growing cells of the H. neptunium wild-type strain were diluted into fresh media containing different concentrations of MP265. Subsequently, their growth was monitored for 30 h using a microplate reader. (B) Effect of MP265 on cell morphology. Cells were grown to exponential phase and exposed for 24 h to 250 µM MP265. After washing and resuspension in medium lacking the inhibitor, cells were cultivated further to monitor the gradual recovery of wild-type morphology. Samples were taken at the indicated time points after addition (+) or removal (-) of MP265 and analyzed by DIC micros¬copy. Aberrant stalks are indicated by arrowheads. Scale bar: 3 µm. (C,D) Quantitative analysis of changes in cell shape after MP265 treatment. Cells were grown to exponential phase and exposed to the indicated concentrations of MP265 for 24 h. After imaging by DIC microscopy, the lengths (C) and widths (D) of their cell bodies (excluding stalks and buds) were measured. The data are shown as box plots, as described in Figure 5C. Distributions significantly different from that of the control culture (0 µM) are indicated (***; t-test, $p < 10\text{-}5$ in C and $p < 10\text{-}17$ in D). n = 100 for each concentration.

94x57mm (300 x 300 DPI)

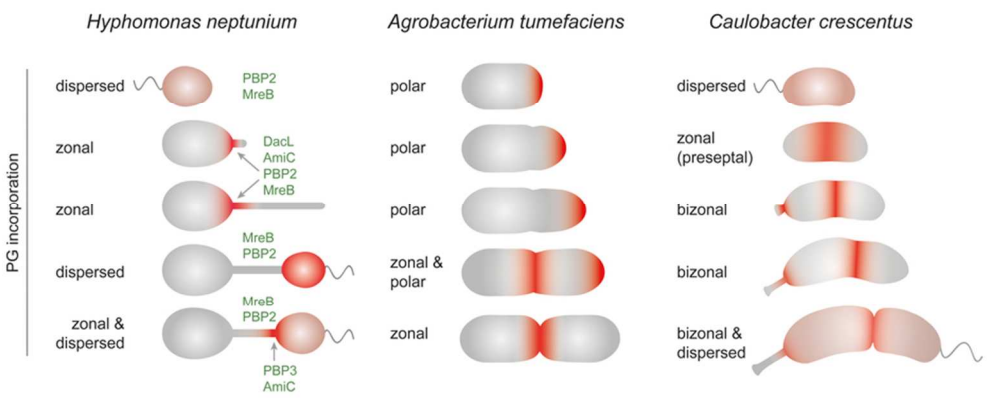

Figure 9. Main growth zones of H. neptunium, A. tumefaciens, and C. crescentus. H. neptunium exhibits four distinct growth zones (red), alternating between disperse and zonal PG incorporation. A. tumefaciens elongates by polar growth and then divides by zonal growth at the cell center (Brown et al., 2012; Cameron et al., 2014). C. crescentus elongates by dispersed and preseptal zonal growth and divides by zonal growth at midcell. Its stalk emerges by zonal growth at the stalk base (Aaron et al., 2007). See text for details.

80x32mm (300 x 300 DPI)